Maser Activity of Organic Molecules toward Sgr B2(N)

Ci Xue, Anthony Remijan, Alexandre Faure, Emmanuel Momjian, Todd R. Hunter, Ryan A. Loomis, Eric Herbst, Brett Mcguire

The Astrophysical Journal, 967:164 (20pp), 2024 June 1 https://doi.org/10.3847/1538-4357/ad4094

Maser Activity of Organic Molecules toward Sgr B2(N)

Ci Xue[1,2], Anthony Remijan[3], Alexandre Faure[4], Emmanuel Momjian[5], Todd R. Hunter[3], Ryan A. Loomis[3], Eric Herbst[2], and Brett McGuire[1,3]
[1] Department of Chemistry, Massachusetts Institute of Technology, Cambridge, MA 02139, USA; cixue@mit.edu
[2] Department of Chemistry, University of Virginia, Charlottesville, VA 22904, USA
[3] National Radio Astronomy Observatory, Charlottesville, VA 22903, USA
[4] Université Grenoble Alpes, CNRS, IPAG, F-38000 Grenoble, France
[5] National Radio Astronomy Observatory, Socorro, NM 87801, USA
Received 2023 July 3; revised 2024 April 11; accepted 2024 April 17; published 2024 May 30

Abstract

At centimeter wavelengths, single-dish observations have suggested that the Sagittarius (Sgr) B2 molecular cloud at the Galactic Center hosts weak maser emission from several organic molecules, including CH_2NH, HNCNH, and $HCOOCH_3$. However, the lack of spatial distribution information on these new maser species has prevented us from assessing the excitation conditions of the maser emission as well as their pumping mechanisms. Here, we present a mapping study toward Sgr B2 north (N) to locate the region where the complex maser emission originates. We report the first detection of the Class I methanol (CH_3OH) maser at 84 GHz and the first interferometric map of the methanimine (CH_2NH) maser at 5.29 GHz toward this region. In addition, we present a tool for modeling and fitting the unsaturated molecular maser signals with non-LTE radiative transfer models and Bayesian analysis using the Markov Chain Monte Carlo approach. These enable us to quantitatively assess the observed spectral profiles. The results suggest a two-chain-clump model for explaining the intense CH_3OH Class I maser emission toward a region with low continuum background radiation. By comparing the spatial origin and extent of maser emission from several molecular species, we find that the 5.29 GHz CH_2NH maser has a close spatial relationship with the 84 GHz CH_3OH Class I masers. This relationship serves as observational evidence to suggest a similar collisional pumping mechanism for these maser transitions.

Unified Astronomy Thesaurus concepts: Interstellar masers (846); Radiative transfer (1335); Galactic center (565); Spectral line identification (2073)

1. Introduction

Maser emission from molecular species has provided critical insights into the kinetic properties of young stars and has even enabled monitoring of their accretion processes (Hunter et al. 2018, and references therein). Energetic events (e.g., outflows and collimated jets) and infrared radiation surrounding massive protostars provide the energy to overpopulate the upper-energy levels of specific molecular transitions and amplify the molecular emission intensities (Moscadelli et al. 2016; Sanna et al. 2016). Common species exhibiting maser emission include, but are not limited to, OH, SiO, H_2O, H_2CO, NH_3, and CH_3OH. An empirical taxonomy based on pumping mechanisms classifies molecular masers into two categories (Batrla et al. 1987; Cyganowski et al. 2009); H_2O and Class I CH_3OH masers are most often excited via collisions and tend to reside in shocked material associated with outflows and expanding H II regions (e.g., Baudry et al. 1974; Elitzur & Fuqua 1989; Voronkov et al. 2014; Towner et al. 2017), while OH and Class II CH_3OH masers are excited via radiation and are generally close to young stellar objects and luminous infrared sources (e.g., Sobolev & Deguchi 1994; Sobolev et al. 1997; Cragg et al. 2002, 2005). The most extensively studied Class I CH_3OH masers include the $4_{-1} - 3_0\,E$ transition at 36 GHz and the $7_0 - 6_1\,A$ transition at 44 GHz, while Class II CH_3OH masers include the $5_1 - 6_0\,A$ transition at 6.7 GHz and the $2_0 - 3_{-1}\,E$ transition at 12.2 GHz (e.g., Voronkov et al. 2014; Song et al. 2022).

By correlating the maser emission from various species with a sample of star-forming regions at different stages, statistical analyses have also suggested that masers may help to trace the evolutionary phases of massive stars (e.g., Figure 6 in Breen et al. 2010). For example, Forster & Caswell (1989) found that isolated H_2O masers tend to appear in sources at earlier evolutionary stages than OH masers based on a survey toward 74 star-forming regions. In addition, Class II CH_3OH masers, which appear exclusively in massive star-forming regions (Xu et al. 2008; Breen et al. 2013), typically have a significant overlapping time line with H_2O masers and arise before the OH masers and ultracompact (UC) H II regions turn on (Walsh et al. 2003; Szymczak et al. 2005).

However, within the picture of massive star formation, the position for Class I CH_3OH masers in an evolutionary sequence is less clear. Initial comparisons of the mid-infrared properties of the sample of CH_3OH maser sources suggested that Class I masers are signposts of the earliest stage of massive star formation, even prior to H_2O masers (Ellingsen 2006). In contrast, detailed mapping of multiple Class I CH_3OH maser transitions toward a luminous young stellar object, IRAS 16547-4247, led Voronkov et al. (2006) to argue that Class I CH_3OH masers can appear earlier than the Class II masers but also last long enough to coexist with the OH masers. Subsequent observations toward the massive protocluster G18.67+0.03 further suggested that the Class I CH_3OH masers might associate with both young sites and relatively evolved UC H II regions within the same protocluster

Table 1
Summary of VLA Observation Parameters

Subband	Frequency Range (MHz)	Channel Number	Spectral Resolution (kHz | km s^{-1})	BWs (MHz)	Synthesized Beam[a]	Targeted Species
5	5282.8–5298.8	1024	15.625 | 0.885	16	3.351 × 1.292	CH_2NH
17	4439.8–4443.8	256	15.625 | 1.05	4	3.983 × 1.542	CH_2NH

Note.
[a] The synthesized beam size obtained with `Natural` weighting.

(Cyganowski et al. 2012). In any case, high angular resolution imaging is essential for determining which protostar(s) within a protocluster currently power these masers (Towner et al. 2017).

Recently, new maser species, such as HNCO and CH_2NH, have been discovered to exhibit compelling roles in inferring fine-scale structures and gas dynamics in the maser region. In particular, the HNCO maser was found to be associated with accretion flows, which helped to build an arm-spiral-structure model of one particular high-mass young stellar object (Chen et al. 2020); and the CH_2NH maser toward galactic nuclei helps to probe the inner nuclear processes in extragalactic environments (Gorski et al. 2021). The pumping mechanism of these new maser species, however, is less constrained, as is their relation to other common maser species. Observations of these species in maser-active regions that contain both known collisionally and radiatively pumped masers are therefore critical as a first step in understanding their pumping mechanisms.

The high-mass star-forming region Sgr B2 north (N) displays rich maser activity from a diverse set of molecules, ranging from common maser species to rare complex molecules (Morita et al. 1992; McGrath et al. 2004; Hoffman et al. 2007; Fujisawa et al. 2014; Qiao et al. 2018). The single-dish PRebiotic Interstellar MOlecular Survey (PRIMOS) project has identified numerous species exhibiting maser activity at centimeter wavelengths. In fact, the discovery of interstellar carbodiimide (HNCNH) was only achievable due to its maser emission (McGuire et al. 2012). Radiative transfer calculations have also revealed that most emission lines of both methyl formate ($HCOOCH_3$) and CH_2NH detected in PRIMOS are weak masers amplifying the background continuum radiation of Sgr B2(N) at centimeter wavelengths (Faure et al. 2014, 2018). However, the large ∼2.′5 × 2.′5 field of view of PRIMOS at the *C* band (∼5 GHz) includes both the north and main components of Sgr B2, complicating the interpretation of the spectral profiles. Therefore, it is crucial to have interferometric observations to disentangle in detail the various possible spatial components of maser emission.

In this work, we present a rigorous imaging study of maser emission from CH_3OH and CH_2NH toward Sgr B2(N). We describe the interferometric observations at centimeter and millimeter wavelengths in Section 2. A description of the methodology employed to model maser emission is described in Section 3, which includes the implementation of a Bayesian inference of physical characteristics. Section 4 presents both the spectra and spatial distribution per maser species. Section 5 contains discussions on the metastable states of maser transitions (Section 5.1), pumping mechanisms inferred from the spatial correlations (Section 5.2), derived physical conditions of masing gas clumps (Section 5.3), and a caveat on modeling maser intensity (Section 5.4).

2. Observations

The interferometric data used here were acquired from two data sets involving the Karl G. Jansky Very Large Array (VLA) in the *C*-band (nominal frequency coverage 4–8 GHz) and the Atacama Large Millimeter/submillimeter Array (ALMA) in Band 3 (nominal frequency coverage 84–116 GHz).

VLA Observations. The VLA observations were carried out on 2016 May 27 (project code: 16A-076, PI: B. McGuire) with the *C*-band receiver. The correlator was configured to deliver 24 subbands or spectral windows, with bandwidths of 4, 8, and 16 MHz, to target various spectral lines. Additionally, nine 128 MHz spectral windows were set up to help with calibration, if needed. The results presented here are based on three spectral windows that delivered channel widths between 0.485 and 2.31 km s^{-1}, depending on the corresponding bandwidth and observing frequency. Detailed observational parameters of each spectral window are presented in Table 1. The phase center of the observations was targeted toward Sgr B2 (N), with the field center at $\alpha_{J2000} = 17^h47^m19.^s80$, $\delta_{J2000} = -28°22'17.''00$. The bandpass and absolute flux density scale calibrator was 3C286, while the complex gain calibrator was J1744-3116. The array was in the *B* configuration with 27 antennas, which covered baselines from 250 m up to 11 km and resulted in the maximum recoverable scale of 37″ at 4 GHz.

The `CASA` software package version 5.6.1 (CASA Team et al. 2022) was used for data reduction and imaging analysis of the VLA observations. For each spectral window, the continuum emission was subtracted in the *uv*-plane before imaging the spectral cubes. We used the `tclean` task with the automasking algorithm for imaging with the natural weighting scheme and a cell size of 0.″27. The resulting size of the synthesized beam (FWHM) of each image cube has a median value of ∼3.″8 × 1.″5. The median of the resultant typical rms noise levels is ∼0.9 mJy beam^{-1}.

ALMA Observations. The ALMA observational data were acquired from the ALMA Science Archive of the survey project entitled "Exploring Molecular Complexity with ALMA (EMoCA)" (project code: 2011.0.00017.S, PI: A. Belloche). A detailed description of the EMoCA data has been presented in Belloche et al. (2016). In this work, two measurement sets, spectral window 0 of setup S1 and spectral window 0 of setup S4 (Xue et al. 2019), were used for imaging the 84 and 95 GHz CH_3OH transitions. Different from Xue et al. (2019), we used the `tclean` task with the automasking algorithm for the imaging analysis, consistent with the VLA imaging process. The resultant synthesized beam size is 2.″23 × 1.″67 at 84 GHz and 1.″94 × 1.″49 at 95 GHz with a median rms value of 4 mJy beam^{-1}.

3. Analysis

In order to constrain the excitation conditions quantitatively, we used the `molsim` program to model the molecular spectra with non-LTE radiative transfer models and to explore the physical parameter space with the Markov Chain Monte Carlo (MCMC) approach (Lee et al. 2023).

3.1. Non-LTE Radiative Transfer Modeling

We implemented the `RADEX` non-LTE radiative transfer code (van der Tak et al. 2007) into `molsim` written in `Python`. The module was accelerated with `Numba` to provide the high performance required for MCMC analysis.

`RADEX` considers a gas clump consisting of a targeted molecular species and its collision partners, such as H_2 and e^-. The gas clump is embedded in a local background radiation field and has a certain geometry (e.g., slab, uniform sphere, expanding sphere). With this physical picture, `RADEX` iteratively solves for the level population by incorporating an equilibrium with inelastic collisions and the local radiation field. Lastly, it computes the peak optical depth, excitation temperature, and peak intensity of each line based on the level population and the line properties, assuming the local radiation field as the only source of background continuum emission. The model can be described with physical parameters, including kinetic temperatures (T_k), densities of collision partners (n_c), background radiation field temperatures (T_{bg}), source velocity (V_{lsr}), line widths (dV), and molecular column densities (N_{col}).

In our implementation, we construct a modification and extend it to support a continuum temperature (T_{cont}) different from the local radiation field temperature (T_{rad}[6]) and allow multiple components to align perfectly along the line of sight (LOS). In the case of a population inversion, T_{cont} serves as background radiation that stimulates the maser gain and is amplified by the foreground gas clump. We assume the continuum source and the gas components to be spatially distant from each other such that the continuum radiation is not included in the excitation analysis and the embedded radiation field of each component is only dominated by the local radiation field. Detailed justifications for this assumption will be discussed in Section 5.3. With this assumption, the level population of each component is computed with a distinct excitation condition using `RADEX`. The frequency-dependent optical depth and source function of the ith component are reconstructed by summing over all lines as follows:

$$\tau_i(\nu) = \sum_j \tau_{i,j}^{\rm peak}\,\phi_i(\nu;\,\nu_{0,j}), \tag{1}$$

$$S_i(\nu) = \frac{\sum_j \tau_{i,j}^{\rm peak}\,\phi_i(\nu;\,\nu_{0,j})B_\nu(T_{{\rm ex},i,j})}{\tau_i}, \tag{2}$$

$$\phi_i(\nu;\,\nu_0) = G\left(\nu;\,\nu_0\left(1-\frac{V_{{\rm lsr},i}}{c}\right),\,\frac{dV_i}{\sqrt{8\ln 2}}\right), \tag{3}$$

$$G(x;\,\mu,\,\sigma) = \exp\left(-\frac{(x-\mu)^2}{2\sigma^2}\right). \tag{4}$$

Here, $\tau_{i,j}^{\rm peak}$ and $T_{{\rm ex},i,j}$ are the optical depth and excitation temperature returned by `RADEX` for the jth line of the ith component, B_ν is the Planck function, ϕ_i is the line profile for the ith component using the Gaussian function G, and τ_i and S_i are the total optical depth and source function with all lines being accounted for.

Using these definitions, for an n-component model where the continuum radiation is first processed by the first component, then the second component and so on, the final intensity with the continuum subtracted can be expressed as

$$I_\nu = B_\nu(T_{\rm cont}) \times \left(e^{-\sum_{i=1}^{n}\tau_i} - 1\right) + \sum_{i=1}^{n} S_i \times (1-e^{-\tau_i}) \times e^{-\sum_{j=i+1}^{n}\tau_j}. \tag{5}$$

In the case of two components, the continuum-subtracted intensity is

$$I_\nu = B_\nu(T_{\rm cont}) \times (e^{-\tau_1-\tau_2} - 1) + S_1 \times (1-e^{-\tau_1}) \times e^{-\tau_2} + S_2 \times (1-e^{-\tau_2}). \tag{6}$$

It is worthwhile to note that the expressions reduce back to that of `RADEX` in the case of one component when the continuum temperature is equal to the local radiation temperature (i.e., $T_{\rm cont} = T_{\rm rad} = T_{\rm bg}$). The calculations in `molsim` reproduces the results returned by RADEX down to machine precision when the results are converged.

In this work, we assume that the local radiation is contributed by the cosmic microwave background only, i.e., $T_{\rm rad} = 2.725$ K (Mather et al. 1999) and a uniform spherical geometry. We only consider H_2 as the collision partner, assuming a kinetic temperature-dependent thermal ortho-to-para ratio (OPR), which can be approximated by

$$\mathrm{OPR}(T_k) = \begin{cases} 9\,e^{-170.6\ \mathrm{K}/T_k} & \text{if } T_k \leqslant 150\ \mathrm{K}, \\ 3 & \text{if } T_k > 150\ \mathrm{K}. \end{cases} \tag{7}$$

We left all the rest as free parameters and allowed them to be fitted using the MCMC approach as described below.

3.2. MCMC Fitting

For line fitting, we used a Bayesian approach to compare models with different parameters and calculate their probability distributions. This approach provides an inference by conditioning the data on priors and sampling posterior distributions. In practice, we use the MCMC approach to explore parameter space.

We use a logarithmic likelihood distribution with the formula below:

$$l = \sum_i \left[-\ln(\sigma_i\sqrt{2\pi}) - \frac{1}{2}\frac{(x_i-\mu_i)^2}{\sigma_i^2}\right] \tag{8}$$

where x is the observed spectral line intensity, μ is the model line intensity, and σ is the uncertainty of the observations including an estimated 10% systematic uncertainty with the standard baseline deviation. The distribution applies to the case where the data set has a nonuniform uncertainty, in which case we compute the uncertainties for each spectral chunk separately.

[6] In `RADEX`, the local radiation temperature is denoted as $T_{\rm bg}$.

The resulting corner plots are shown in Appendix B. A corner plot shows the probability distribution for each pair of parameters and for each parameter individually. In the following, the fitted results are represented by the 50th, 16th, and 84th percentiles as the representation value and the range of uncertainty, also known as the 68% confidence interval. This choice is equivalent to choosing the mean and $\pm1\sigma$ for a normal distribution, which is the case for most of our posterior distributions. One of the advantages of the MCMC technique over a traditional least-squares fit approach is that a larger parameter space can be explored more efficiently. Rather than only returning the parameters that maximize the likelihood function (e.g., least-squares fitting),[7] it returns the actual probability of the parameters, which can be used to assess whether parameters are highly covariant with one another. The correlation between parameters manifests itself as nonseparable distributions in the corner plots.

4. Results

We investigate the maser activities of two transitions in this work. The detailed spectroscopic parameters for each maser transition along with the observational results of the corresponding emission features are summarized in Table 2. For CH_3OH, we examined the molecular spectra extracted toward two distinct regions, maser spot 1 (MS1, $\alpha_{J2000} = 17^h47^m19\overset{s}{.}730$, $\delta_{J2000} = -28°22'04\overset{''}{.}580$) and maser spot 2 (MS2, $\alpha_{J2000} = 17^h47^m20\overset{s}{.}393$, $\delta_{J2000} = -28°22'12\overset{''}{.}410$). Toward both regions, we performed MCMC analyses with a two-chained-component model, as presented in Section 4.1.1 for MS1 and 4.1.2 for MS2, respectively. For CH_2NH, as there is no detectable signal toward MS1, we examined its spectrum extracted toward MS2 only and performed the MCMC analysis with a one-component model as presented in Section 4.2.

Empirically, a brightness temperature (T_B) of an emission line much greater than the source physical (kinetic) temperature is considered as an indication of a maser emission rather than a thermally excited line (Voronkov et al. 2006; Gargaud et al. 2011). As elaborated in the following sections, our MCMC analyses suggest the T_k for the masing clumps in Sgr B2(N) to be ∼29–37 K. In contrast, as summarized in Table 2, the observed T_B values of the molecular emission investigated in this work (>120 K) are significantly higher than the physical temperatures. Furthermore, we also performed a spectral analysis assuming a single excitation temperature to equal T_k for comparison and found that the observed spectral profiles deviate substantially from the thermal model. Additional evidence for maser activities, including the non-Gaussian shape of line profiles, the compact emitting regions, the negative opacity values, and the metastable upper-energy levels, will be discussed further in the following sections. All combine to support the observed emission of CH_3OH at 84 GHz toward both MS1 and MS2 and CH_2NH at 5.29 GHz toward MS2 to consist of astronomical (weak) masers.

As a reference for the relative positions, Figure 1 shows the continuum emission from Sgr B2(N) observed at 6.8 cm (left) and 3.5 mm (right). The free–free continuum emission concentrations at 6.8 cm include four cores, K1–K4, and the two bow-shaped H II regions, K5 and K6 (Corby et al. 2015, marked in green in Figure 1). At 3.5 mm, three main hot cores, N1–N3, were revealed by their molecular emission (Bonfand et al. 2017, marked in orange in Figure 1).

4.1. Class I CH_3OH Masers

Class I CH_3OH masers are prevalent in massive star formation regions. In particular, the 44 GHz maser line was observed toward Sgr B2 at 3″ resolution (Mehringer & Menten 1997). In contrast, there is limited information about the $5_{-1} - 4_0\,E$ Class I CH_3OH maser at 84 GHz, a member of the same $J + 1_{-1} - J_0\,E$-type transition family along with the 36 GHz line (Breen et al. 2019, and references therein). Interferometric observations of the 84 GHz line in the Milky Way are even rarer (Voronkov et al. 2006), as recent work has focused on extragalactic detections (McCarthy et al. 2018; Humire et al. 2022).

Here, we present the first interferometric ALMA observations of the 84 GHz CH_3OH masers in a Milky Way object at a resolution of 1.″5, as well as the first detection of the 84 GHz maser toward Sgr B2. The spread of 84 GHz maser spots is manifest in the channel images shown in Figure 2, with velocities ranging from 50–86 km s^{-1}. The brightest maser spot located ∼3.″6 west of the K4 core with a V_{lsr} of 58 km s^{-1} (hereafter referred to as MS1) has a peak T_B of 389.2 ± 0.2 K (8.454 ± 0.004 Jy beam^{-1}, Figures 2 (q)–(t)). In addition to the brightest spot MS1, another maser knot associated with the K6 H II region is also identified with a T_B of 75.4 ± 0.4 K (1.636 ± 0.008 Jy beam^{-1}) at a V_{lsr} of 83 km s^{-1} (hereafter referred to as MS2), as shown in Figures 2 (b)–(e).

The molecular data file for E-type CH_3OH was taken from the Excitation of Molecules and Atoms for Astrophysics (EMAA) database,[8] with spectroscopy from the Cologne Database for Molecular Spectroscopy (CDMS) catalog[9] (Müller et al. 2005) and collision rate coefficients reported by Rabli & Flower (2010) for the rotational excitation of CH_3OH by para- and ortho-H_2 (hereafter p-H_2 and o-H_2). The calculations of Rabli & Flower (2010) were performed for rotational transitions within the three first torsional states of CH_3OH, $\nu = 0$, 1, 2, with a CH_3OH basis including rotational states $j_1 \leqslant 15$ for p-H_2($j_2 = 0$) and $j_1 \leqslant 9$ for o-H_2($j_2 = 1$), where j_1 and j_2 are the rotational quantum numbers. The coupled-states approximation was used to generate rate coefficients at temperatures $10 \leqslant T_k \leqslant 200$ K. Because torsionally inelastic transitions were not considered by Rabli & Flower (2010), the EMAA data set for E-CH_3OH includes rotational transitions within the ground torsional state ($\nu = 0$) only. The first excited state ($\nu = 1$) of E-CH_3OH opening at 204.2 cm^{-1}, the highest level of E-CH_3OH included in the EMAA data set is the rotational state 9_{-6} ($j_1 = 9$, $K = -6$) with an energy of 203.9 cm^{-1}.

4.1.1. Masers with Dark Continuum Background—MS1

Four uncontaminated E-type CH_3OH transitions covered in the collision data were used to constrain the physical parameters quantitatively using a non-LTE model and MCMC fitting algorithm. The observed spectra extracted toward the brightest maser spot MS1 are shown in Figure 4. We first attempted with a single-clump model but found that the

[7] When the posteriors deviate from a Gaussian distribution, the parameters exhibiting the highest likelihood may not necessarily correspond to the optimal parameters.

[8] https://emaa.osug.fr

[9] https://cdms.astro.uni-koeln.de

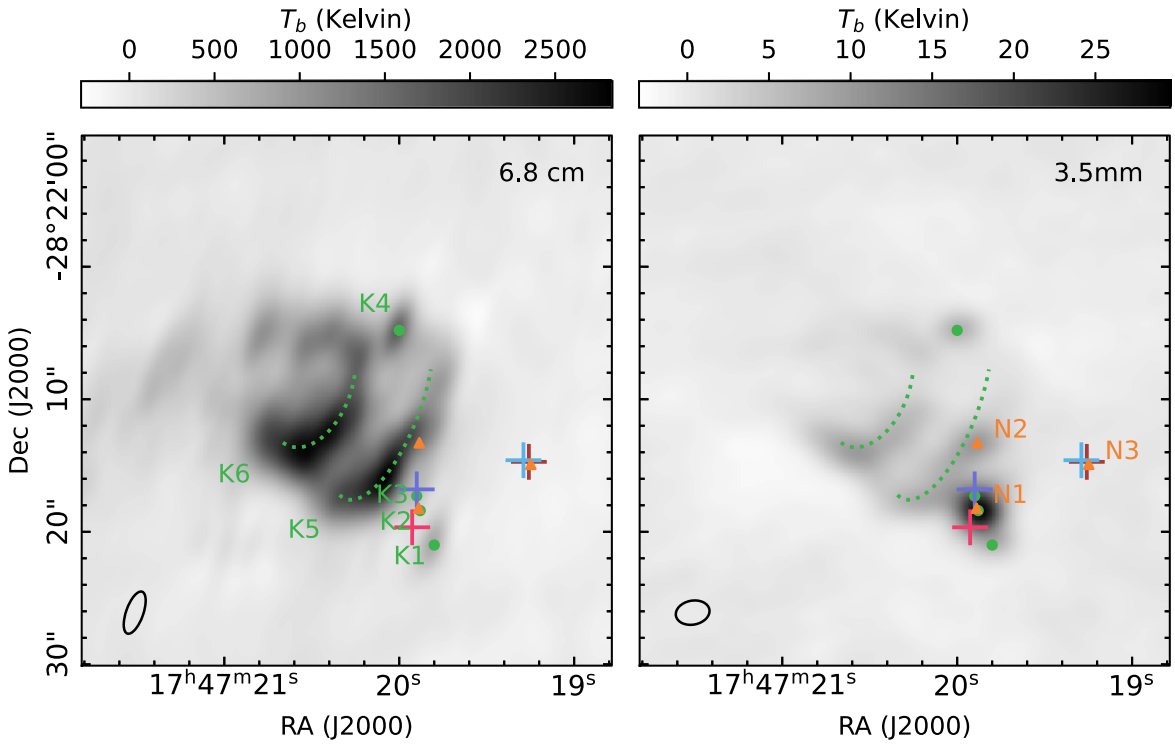

Figure 1. Continuum emission toward the Sgr B2(N) region obtained with the VLA at 6.8 cm and ALMA at 3.5 mm. The centimeter-wave emission concentrations (K1–K6, Corby et al. 2015) are indicated by green dashed lines and circle markers, whereas the molecular hot cores identified in millimeters (N1–N3, Bonfand et al. 2017) are indicated by orange triangle markers. The + symbols mark the location of Class II CH_3OH masers in blue, the brightest maser spots are marked in rose for the H_2O maser (Walsh et al. 2014), in purple for the OH maser (Argon et al. 2000), and in firebrick for the NH_3 maser (Yan et al. 2022).

Table 2
Investigated Maser Transitions

Molecule	Rest Frequency (MHz)	Transition		E_u (K)	$S_{ij}\mu^2$ (D^2)	$\log_{10}\frac{A_{ul}}{s^{-1}}$	$T_{B,\,peak}$[a] (K)	T_{ex} (K)	τ
CH_3OH	84521.172(12)	$5_{-1}-4_0\,E$	⋯	40.4	12.332	−5.6979	389.2 ± 0.2	−5.8[b]	−2.44[b]
CH_2NH	5288.962(3)	$1_{1,0}-1_{1,1}$,	$F=0-1$	11.1	0.897	−8.8109	$\geqslant 121.8 \pm 8.6$	−0.62[c]	−0.008[c]
	5289.712(3)	⋯	$F=1-0$	⋯	0.897	−9.2881	⋯	−0.54[c]	−0.009[c]
	5289.815(3)	⋯	$F=2-2$	⋯	3.365	−8.9357	⋯	−0.65[c]	−0.030[c]
	5290.671(3)	⋯	$F=2-1$	⋯	1.121	−9.4125	⋯	−0.55[c]	−0.011[c]
	5290.828(3)	⋯	$F=1-2$	⋯	1.122	−9.1908	⋯	−0.75[c]	−0.008[c]
	5291.682(3)	⋯	$F=1-1$	⋯	0.673	−9.4124	⋯	−0.62[c]	−0.006[c]

Notes.
[a] Peak brightness temperature measured at the brightest emission spot for each molecule. The brightest emission spot for 84 GHz CH_3OH Class I maser is located near the K4 core at a V_{lsr} of 58 km s^{-1}. The brightest emission spot for 5.29 GHz CH_2NH maser is located in the K6 H II region at a V_{lsr} of 83 km s^{-1}. The measured T_B of CH_2NH represents a lower limit to the $T_{B,\,peak}$ because of the limited angular resolution of the VLA observations.
[b] Characteristics of the CH_3OH foreground masing clump toward MS1.
[c] Characteristics of the CH_2NH masing gas toward MS2.

observed spectra could not be reproduced with physically realistic parameters even after relaxing the constraints on T_{cont} and T_{rad}. In order to match the bright maser emission at 84.5 GHz, strong background radiation is needed to stimulate the maser gain in the single-clump model but it will also introduce significant absorption features at both 85.5 and 108.9 GHz.

Moreover, as shown in Figure 2(r), there is no significant millimeter-wave continuum source at MS1. While this spot also exhibits a strong CH_3OH emission at 44 GHz ($T_B = 157$ K, Mehringer & Menten 1997), it shows no continuum emission at centimeter wavelengths either. The closest continuum source, K4, is offset by ∼3.″6, which corresponds to ∼0.14 pc at the distance of Sgr B2 (8.2 kpc, Reid et al. 2019). In addition, as shown in Appendix A, there are no point sources associated with this maser spot. The nearest bright infrared source observed with both the Two Micron All Sky Survey (2MASS) and the Galactic Legacy Infrared Midplane Survey Extraordinaire (GLIMPSE) program is located at ∼5.″2 to the west of the maser spot. Instead, the background radiation stimulating the maser gain may be weak and diffuse, causing it to be resolved out by interferometers, such as the free–free and dust emission in the Galactic plane.

As illustrated in Figure 3, the model we consider consists of two-chained gas clumps overlapping in velocity along the LOS, where the foreground clump exhibits maser activity but the

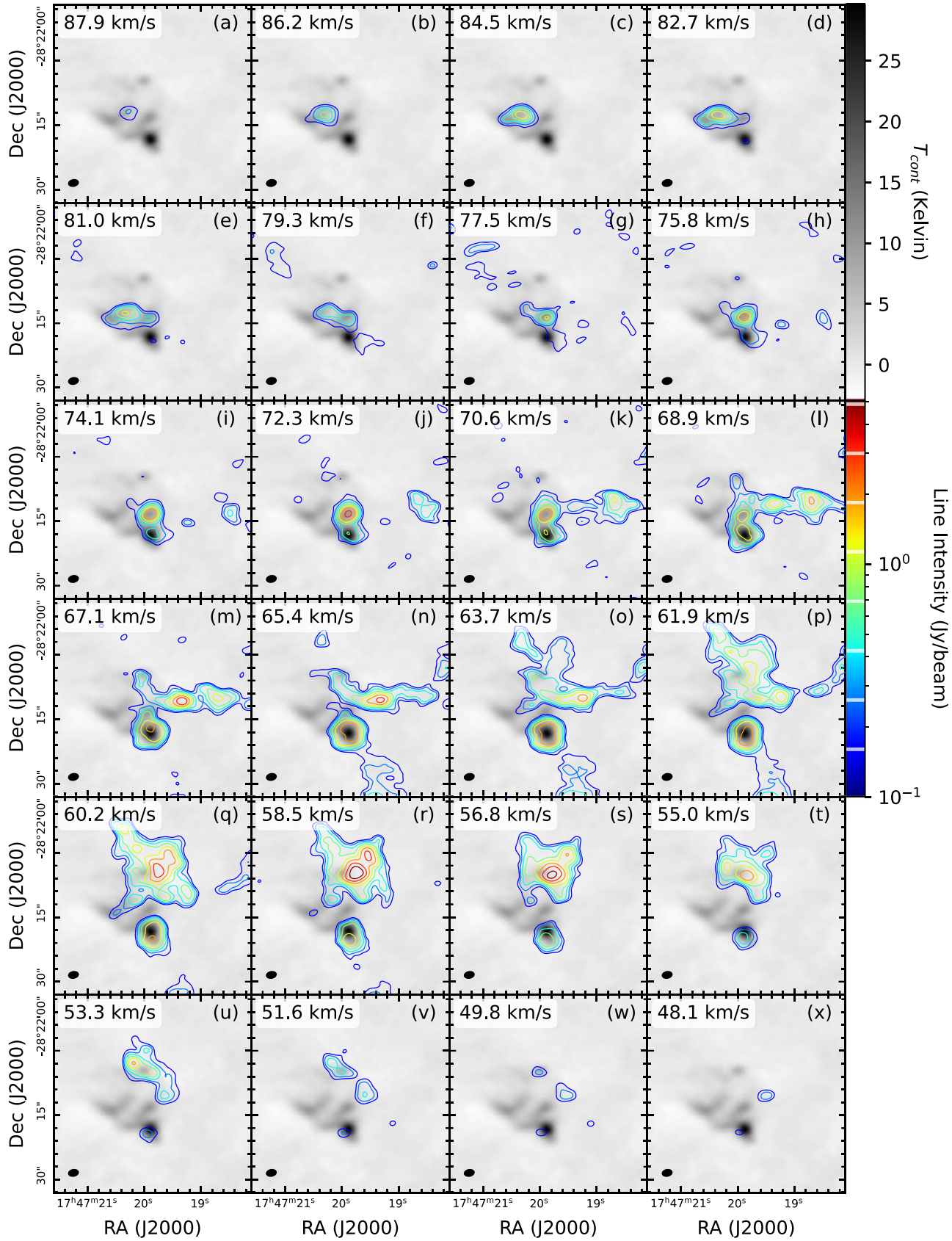

Figure 2. Channel maps of the Class I CH_3OH maser at 84 GHz overlaid on the continuum emission observed at 3.5 mm. The contours levels are 4.0 mJy beam^{-1}(1σ) × (40, 65, 106, 173, 282, 459, 749, 1220). The peak value is 8.45 Jy beam^{-1}.

background clump can either be also an inverted maser (i.e., the double-maser scenario) or noninverted emitting (i.e., the single-maser scenario). In both scenarios, this model can account for the strong maser emission with an absence of a bright and compact continuum source. It is analogous to the "self-amplification" model of two masing clouds that has been used to interpret water megamasers observed in circumnuclear disks in active galactic nuclei (Kartje et al. 1999).

A chained two-component model has been constructed to iteratively generate synthetic spectra, each component being described with five parameters, T_k, n_c, N_{col}, dV, and V_{lsr}. We assumed the two components have coherent but not identical values of V_{lsr} of $\sim$58 km s^{-1}, although spatially separated along the LOS. As such, two V_{lsr} parameters have the same prior probability distributions but are fit independently. Including both V_{lsr} values, the priors for the free parameters and the MCMC analysis are discussed in detail in Appendix B. Posterior probability distributions for each parameter and their covariances were generated with 100 walkers with 50,000 samples each.[10]

As revealed in the bimodal posterior distributions, the samples converge toward two distinct peaks, each corresponding to the double-maser and single-maser scenarios, respectively. The statistics of the resulting parameters for each scenario were summarized in Table 3, which were used to construct the synthetic spectra for the double-maser scenario shown with the green trace and the single-maser scenario shown with the purple trace in Figure 4. Both synthetic profiles well reproduce the observed spectra, capturing both the maser and the optically thick emission features. Our model, unfortunately, falls short in matching the low-frequency side of the emission plateau at 108.87 GHz, corresponding to the $0_0 - 1_{-1}$ transition at a velocity range of 70–90 km s^{-1}. This divergence from the observed spectrum implies the potential presence of another optically thick velocity component(s) along the LOS. Because neither of the two scenarios completely reproduces the observed data, it is noteworthy that the uncertainties derived from the MCMC results should be considered as a lower limit of the uncertainties.

In the double-maser scenario, the τ and T_{ex} of the $5_{-1} - 4_0$ maser transition are found to be -2.44 and -5.8 K for the foreground clump and -0.02 and -2027.3 K for the background clump. In the single-maser scenario, the corresponding τ and T_{ex} values are -2.52 and -6.5 K for the foreground clump and 0.13 and 245.2 K for the background clump. As a T_{ex} of 245.2 K is significantly higher than the T_k value in this case, it is evident that this transition exhibits strong noninverted emission and is on the verge of a population inversion.

4.1.2. Masers with Bright Continuum Background—MS2

In contrast to MS1, MS2 is aligned with the K6 H II region along the LOS, which provides background radiation to be amplified by the stimulated emission (Figure 2(d)). The spectra extracted toward MS2 are shown in Figure 6 with two individual velocity components being identified for each of the spectral features. We also performed the spectral analysis for MS2 with a two-component model, where each component has a distinct V_{lsr}.

[10] Each walker represents a Markov Chain consisting of multiple samples with each sample being randomly sampled within the parameter space.

The adopted prior and resultant posterior probability distributions for each parameter are depicted, respectively, in Figure 5. The priors for V_{lsr} were chosen to be Gaussian distributions centering on 83 and 63 km s^{-1}, respectively, based on the difference between the observed sky frequency and the rest frequency. Meanwhile, the T_{cont} prior also has a Gaussian distribution, based on the measured continuum level of 6.67 ± 0.52 K. The remaining parameters all have uninformative uniformly distributed priors. Following 100 walkers with 10,000 samples each, all parameters converge to primarily Gaussian-like distributions in our model. The corresponding corner plot of the posterior distributions and the parameter covariances are shown in Appendix B, with the largest covariance observed between H_2 densities and CH_3OH column densities. This covariance aligns with the fact that H_2 densities and CH_3OH column densities are related through the maser emission measure, $\xi \propto n_c \times N_{col}$, which, together with temperature, determines the overall rate coefficient for a collisionally pumped maser transition (Leurini et al. 2016).

The posterior medians from the MCMC inference (Table 4) were used to construct the synthetic spectra shown in Figure 6. If we take the noise level measured in each passband into account, the synthetic spectral profiles fit satisfactorily with the observed spectra for both the maser and optically thick absorption features. However, the low-velocity component (64 km s^{-1}) of the $6_{-2} - 7_{-1}$ transition fails to match the observed absorption feature at 85.55 GHz. This absorption feature might be attributed to potential contamination from an unidentified transition. The excitation temperature and opacity of the $5_{-1} - 4_0$ maser transition were found to be negative, i.e., -5.6 K of T_{ex} and -2.52 of τ for the high-velocity component (83 km s^{-1}), confirming its maser activity toward MS2.

4.2. CH_2NH Masers

The maser activity of the $1_{1,0} - 1_{1,1}$ CH_2NH transitions at 5.29 GHz has been revealed toward both the Galactic Center and external galaxies as point source emission (Faure et al. 2018; Gorski et al. 2021). With the VLA observations, we resolve this emission spatially into three velocity components with a V_{lsr} of 64, 73, and 83 km s^{-1}. The peak intensity map for each component is shown in Figure 7, respectively. The 83 and 64 km s^{-1} components are both associated with the K6 H II region, while the 73 km s^{-1} component is concentrated toward the K5 H II region. The brightest 83 km s^{-1} component displays a more compact distribution than the other two components, with a T_B of 121.8 ± 8.6 K (12.1 ± 0.85 mJy beam^{-1}). This measured T_B represents a lower limit to the peak T_B since the observed emission morphology of the 83 km s^{-1} component may result from point sources convolved with the coarse VLA beam. Nevertheless, this component of the CH_2NH emission is coherent with that of the 84 GHz CH_3OH maser emission both in the velocity domain and spatial position. Therefore, the significant brightness, highly compact morphology, and coherence with other maser emission suggest maser activity in the 83 km s^{-1} component.

The molecular data file for CH_2NH was taken from the EMAA database. Extended from the calculations in Faure et al. (2018), we calculated the collisional data for rotational transitions of CH_2NH among the first 49 rotational levels, i.e., up to the state $8_{2,6}$ at 99.5 cm^{-1}, and for kinetic temperatures in the range of 10–150 K. The detailed

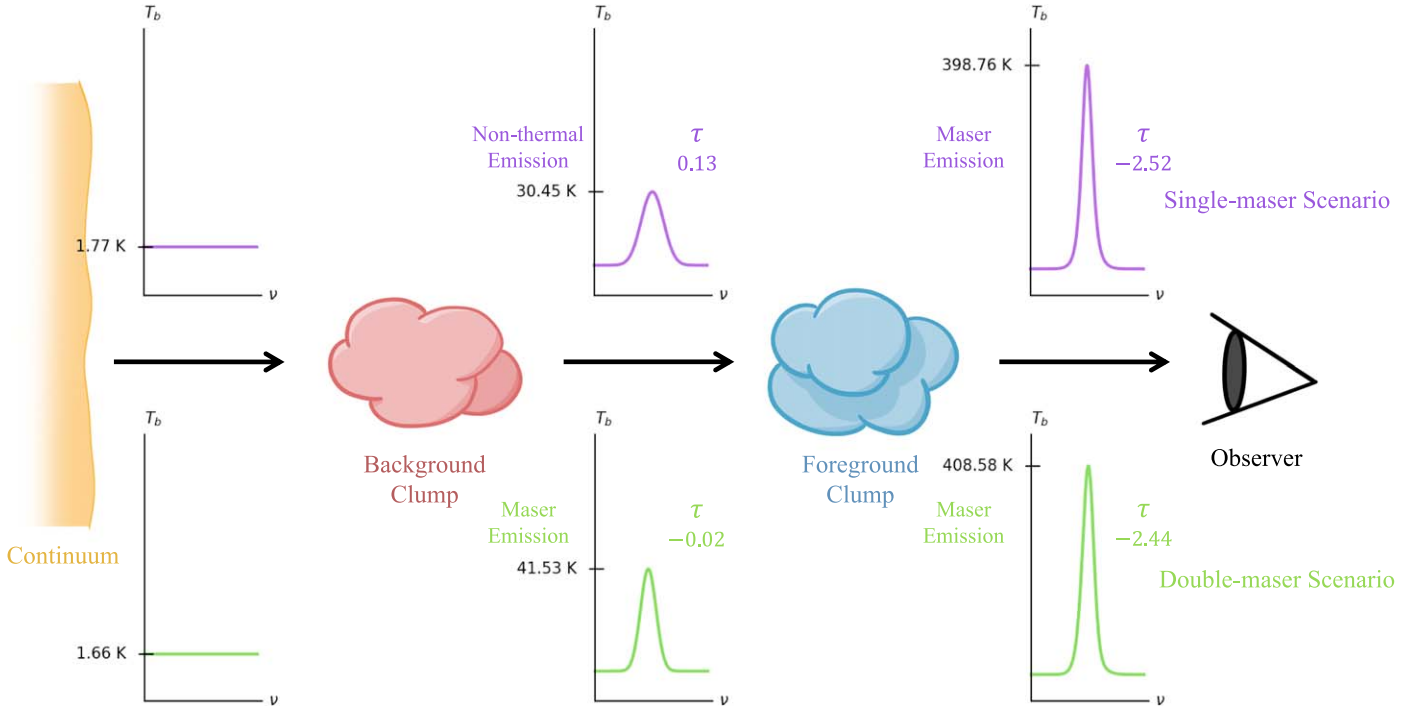

Figure 3. Schematic showing two scenarios of the two-chain-clump model for the 84 GHz CH_3OH maser, where relatively weak continuum radiation passes through two velocity-coherent gas clumps along the LOS, resulting in accumulated maser gains. In the double-maser scenario, the continuum radiation is initially amplified by the background masing clump, followed by further amplification by the foreground masing clump. In the single-maser scenario, however, the foreground masing clump amplifies the noninverted line emission from the background clump. The peak brightness temperature (T_b) and the corresponding optical depth (τ) are annotated in each spectrum.

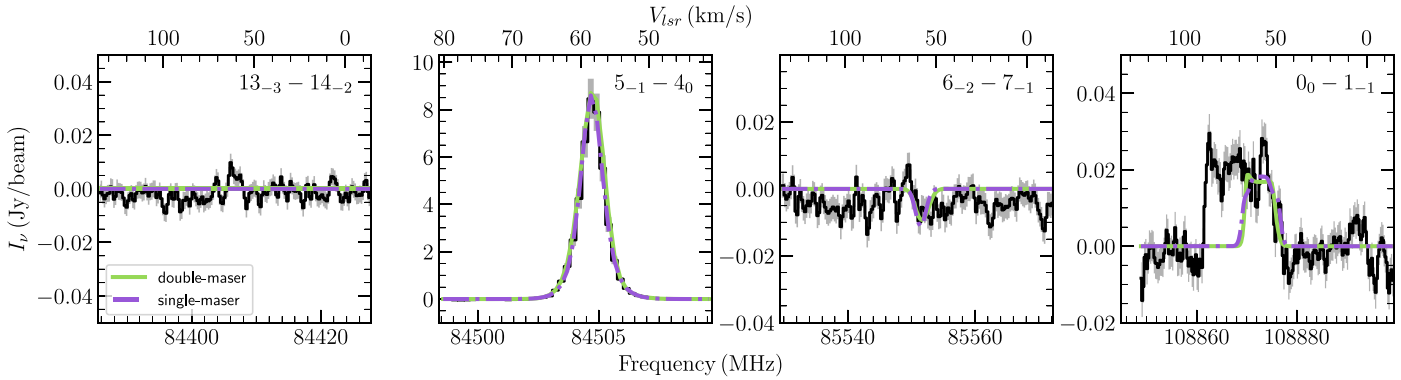

Figure 4. Observed spectra of the *E*-type CH_3OH transitions extracted toward MS1 are shown in black with noise levels shaded in gray. Quantum numbers are given at the top right of each panel. The synthetic spectra are overlaid in colors for different scenarios, with the green trace representing the double-maser scenario and the purple trace representing the single-maser scenario. See Table 3.

Table 3
Summary Statistics of the Marginalized Posterior toward MS1

Two-chain-clump Model	T_k (K)	n_c[a] (cm^{-3})	V_{lsr}[b] (km s^{-1})	dV (km s^{-1})	N_{col} (10^{16} cm^{-2})	T_{cont}[c] (K)
Single-maser scenario[d]	…	…	…	…	…	$3.4^{+0.1}_{-0.1}$
Background	$29.2^{+5.7}_{-5.6}$	$1.4^{+0.6}_{-0.4} \times 10^3$	$57.9^{+0.1}_{-0.1}$	$8.1^{+0.2}_{-0.2}$	$12.1^{+2.6}_{-1.3}$	…
Foreground	$31.9^{+5.8}_{-4.4}$	$5.3^{+2.0}_{-1.6} \times 10^4$	$58.5^{+0.1}_{-0.1}$	$6.2^{+0.2}_{-0.2}$	$1.3^{+0.2}_{-0.2}$	…
Double-maser scenario[d]	…	…	…	…	…	$3.3^{+0.2}_{-0.1}$
Background	$29.3^{+11.2}_{-8.8}$	$2.1^{+2.1}_{-0.8} \times 10^3$	$59.4^{+0.2}_{-0.3}$	$5.8^{+0.2}_{-0.2}$	$8.1^{+1.5}_{-1.3}$	…
Foreground	$32.2^{+5.9}_{-4.8}$	$5.1^{+2.5}_{-2.0} \times 10^4$	$57.3^{+0.2}_{-0.2}$	$8.0^{+0.3}_{-0.3}$	$1.5^{+0.4}_{-0.2}$	…

Notes. The quoted uncertainties represent the 16th and 84th percentiles (1σ for a Gaussian distribution) uncertainties.
[a] n_c represents the number density of the collision partners, which we take to be n_{H_2} as hydrogen is assumed to be the dominant partner.
[b] Two velocity components have similar V_{lsr} of ∼58 km s^{-1} along the LOS.
[c] Continuum temperature for the 84–109 GHz band.
[d] The MCMC analysis revealed two distinct peaks in the posterior distributions, each representing one of the two scenarios. Depending on the scenario, the background clump exhibits maser or noninverted emission, while the foreground clump always exhibits maser emission.

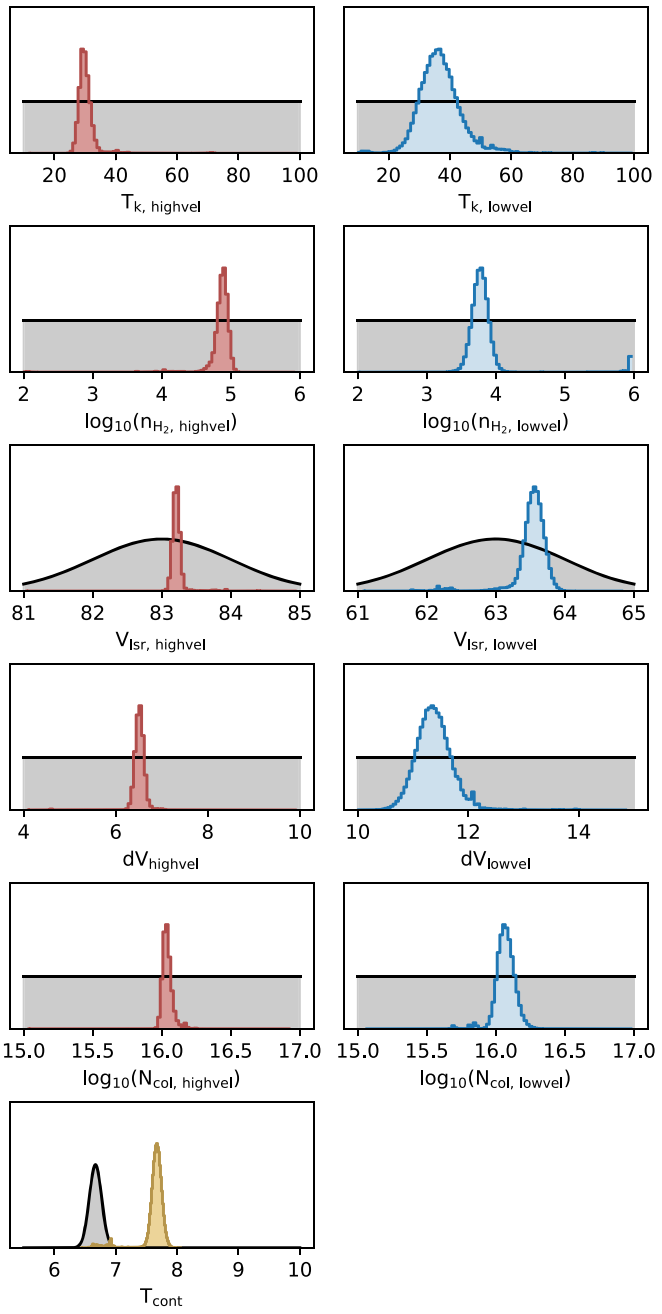

Figure 5. Prior and posterior distributions for the MCMC fit of CH_3OH *E*-type transitions toward MS2. The prior distribution of each parameter is shown in gray. The posterior distributions for the low-velocity component are shown in blue, whereas those for the high-velocity component are shown in red. The posterior of T_{cont} is shown in yellow. The discrepancy of T_{cont} in the posterior relative to the prior could be attributed to a certain portion of continuum flux, especially from extended components, being resolved out by ALMA.

calculations of the collisional rate coefficients are presented in Appendix C.

We performed the MCMC analysis with a one-component model using the prior probability distributions depicted in Figure B4. The VLA observations only cover two transitions of CH_2NH, while the other transition at 4.44 GHz has no signal over the noise levels. As such, the data are insufficient to simultaneously constrain the physical characteristics so the CH_2NH MCMC analysis requires a confined choice of priors on some parameters. We opted to use *E*-type CH_3OH discussed in Section 4.1.2 for physical constraints, where the 83 km s^{-1} components between CH_3OH and CH_2NH are spatially coherent and are both associated with the K6 H II region. We therefore extracted the CH_2NH spectrum toward the same position as MS2. The posteriors on T_k and n_{H_2} obtained from CH_3OH (Table 4; Figure 5; Figure B3) are adopted as MCMC priors for the CH_2NH model. The priors for V_{lsr} and dV are chosen to be Gaussian distributions, informed by the strongest emission feature (12σ) detected in the data. The Gaussian prior for T_{cont} is based on the continuum level of 2687 ± 58 K measured by the VLA. Meanwhile, the N_{col} of CH_2NH has a noninformative uniformly distributed prior.

As shown in the posterior distributions in Figure B4, following 10,000 samples with each of the 100 walkers, the samplers converge at an N_{col} of $4.76^{+1.09}_{-0.64} \times 10^{14}$ cm^{-2}. The synthetic line profile is shown in Figure 8, reproducing six hyperfine components of the $1_{1,0} - 1_{1,1}$ transition within the noise level. The six hyperfine components have T_{ex} in the range of -0.75 to -0.55 K, τ's in the range of -0.03 to -0.006, and, in particular, the $F = 2 - 2$ transition has a T_{ex} of -0.65 K and a τ of -0.03.

5. Discussion

5.1. Metastable Energy Levels of Maser Transitions

The majority of the molecular lines observed toward the H II regions in Sgr B2(N) are in absorption (Corby et al. 2015, and references therein). In contrast, specific transitions of certain species toward these regions exhibit emission features (e.g., McGuire et al. 2012; Corby et al. 2015; Remijan et al. 2022). These transitions establish population inversions between energy levels ($n_{up}g_{low} > n_{low}g_{up}$), a prerequisite for maser action to occur. The mechanism of population inversion is conceptualized by spontaneous decay and collisions: spontaneous decay populates the levels determined by the Einstein coefficients, meanwhile collisions redistribute molecules due to their specific geometry and rotational energy level patterns. Figures 9 and 10 show the energy level structure of spontaneous transitions connected to the two target maser transitions, with Einstein spontaneous emission coefficients (A_{ij}) shown in colors.

In the case of the CH_3OH $5_{-1} - 4_0\,E$ transition at 84 GHz, the upper-energy level $5_{-1}\,E$ is fed by the other higher levels with strong landing transitions but spontaneously decays to the lower-energy level $4_0\,E$ with a weak escaping transition .[11] $5_{-1}\,E$ has a total escaping $\log_{10} A_{ij}/\mathrm{s}^{-1}$ of -4.2139 (equivalent to a lifetime of $\sim 1.6 \times 10^4$ s), which is ~ 3.0 orders of magnitude lower than its total landing A_{ij}. As discussed in Lees (1973) and Menten (1991), CH_3OH spontaneously decays more rapidly within the $K = -1$ stack as compared with decaying out of the $K = -1$ stack. Specifically, among the two escaping transitions, $5_{-1} - 4_{-1}\,E$ is stronger than $5_{-1} - 4_0\,E$ (Figure 9). In fact, the $K = -1$ levels are the endpoints for all spontaneous decay routes (Lees 1973). For example, the lower-energy level of this maser transition ($4_0\,E$) decays rapidly to the lower $K = -1$ levels.

In addition to the spontaneous decay, collisions redistribute molecules over the vertical stacks of the $K = -1$ levels because the $\Delta K = 0$ collisions are preferred compared with $|\Delta K| = 1$ and

[11] An escaping transition refers to a transition in which the upper-energy level is the target energy level, while a landing transition refers to a transition in which the lower-energy level is the target energy level.

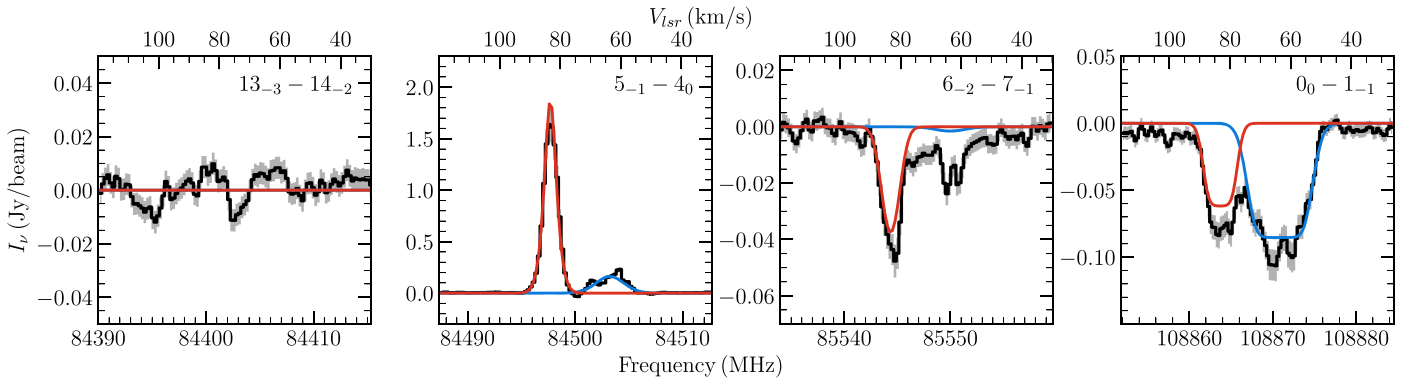

Figure 6. Observed spectra of the *E*-type CH_3OH transitions extracted toward MS2 are shown in black with noise levels shaded in gray. Quantum numbers are given at the top right of each panel. The rest frequency for each transition is 84423.769, 84521.172, 85568.131, and 108893.945 MHz from left to right. The synthetic spectra are overlaid in colors, with the red trace representing the high-velocity component (83 km s^{-1}) and the blue trace representing the low-velocity component (64 km s^{-1}). See Table 4.

Table 4
Summary of the Statistics of the Marginalized Posterior toward MS2

Molecule	T_k (K)	n_c (cm^{-3})	V_{lsr}[a] (km s^{-1})	dV (km s^{-1})	N_{col} (cm^{-2})	T_{cont} (K)
CH_3OH	…	…	…	…	…	$7.7^{+0.1}_{-0.1}$[b]
	$30.7^{+2.0}_{-1.5}$	$8.3^{+1.5}_{-1.6} \times 10^4$	$83.3^{+0.1}_{-0.1}$	$6.6^{+0.1}_{-0.1}$	$1.1^{+0.1}_{-0.1} \times 10^{16}$	…
	$37.3^{+6.4}_{-5.6}$	$6.6^{+2.1}_{-1.5} \times 10^3$	$63.6^{+0.1}_{-0.2}$	$11.4^{+0.3}_{-0.3}$	$1.2^{+0.2}_{-0.2} \times 10^{16}$	…
CH_2NH	…	…	…	…	…	$2687.6^{+62.4}_{-62.4}$[c]
	$31.3^{+4.3}_{-4.3}$	$6.2^{+3.7}_{-2.4} \times 10^4$	$83.5^{+0.3}_{-0.3}$	$7.7^{+0.5}_{-0.5}$	$4.8^{+1.1}_{-0.6} \times 10^{14}$	…

Notes. Similar to Table 3.
[a] Two velocity components are identified along the LOS at a V_{lsr} of 83 and 64 km s^{-1}, respectively.
[b] Continuum temperature for the 84–109 GHz band.
[c] Continuum temperature at 5 GHz.

2 (Menten 1991). In particular, at a T_k of 30 K, the total rate coefficient of the $\Delta K = 0$ collisions de-populating a $K = -1$ level ($\sim 1 \times 10^{-9}$ cm^{3}s^{-1}) is almost two orders of magnitudes higher than that of the $|\Delta K| = 1$ collisions ($\sim 5 \times 10^{-11}$ cm^{3}s^{-1}) and the $|\Delta K| = 2$ collisions ($\sim 3 \times 10^{-11}$ cm^{3}s^{-1}).

For CH_2NH, we sum the hyperfine components of the ^{14}N splittings and use the sum of A_{ij} as the representative A_{ij} for each transition in Figure 10. In the case of the CH_2NH $1_{1,0} - 1_{1,1}$ transition at 5.29 GHz, the upper-energy level $1_{1,0}$ is coupled to the higher levels $2_{1,1}$ and $2_{2,1}$ with strong spontaneous transitions but to the lower-energy level $1_{1,1}$ with a weak escaping transition. Compared with the upper-energy level $1_{1,0}$, which has a total escaping $\log_{10} A_{ij}/s^{-1}$ of -4.2476, (equivalent to a lifetime of $\sim 1.8 \times 10^4$ s), the lower-energy level $1_{1,1}$ has a slightly stronger escaping $\log_{10} A_{ij}/s^{-1}$ of -4.0303 (equivalent to a shorter lifetime of $\sim 1.1 \times 10^4$ s).

Meanwhile, collisions of CH_2NH exhibit a propensity for the $|\Delta K_a| = 0$ transitions compared with the inter-stack transitions $|\Delta K_a| = 1$ and 2 (Faure et al. 2018). In particular, the total rate coefficient of the $\Delta K_a = 0$ collisions de-populating a $K_a = 1$ level ($\sim 10^{-10}$ cm^{3}s^{-1}) is 1 order of magnitude higher than that of the $|\Delta K_a| = 1$ and 2 collisions at a T_k of 30 K. However, the inter-stack transitions from the ground state $0_{0,0}$ complicate this multilevel system. The collisions from $0_{0,0}$ more efficiently populate the lower level $1_{1,1}$ than the upper level $1_{1,0}$, suppressing the inversion. Therefore, while these energy structures allow the temporary trapping of the population in the metastable $1_{1,0}$ level, it only results in a weak population inversion.

5.2. Spatial Origin and Pumping Mechanism

The maser activity of several simple species was reported previously toward Sgr B2(N) with precise locations, including CH_3OH, H_2O, OH, and NH_3, which are indicated by + symbols in Figures 1 and 11. The Class II CH_3OH maser spot at 6.7 GHz is spatially associated with the N3 millimeter-wave core (Caswell 1996; Caswell et al. 2010). A survey performed with the Australia Telescope Compact Array characterized 30 H_2O maser spots with the majority of them located within the N1-K2-K3 region (Walsh et al. 2014). Six OH maser spots have been identified with a VLA survey of OH masers, with the brightest spot being associated with the K3 centimeter-wave core (Argon et al. 2000; Qiao et al. 2014). In a recent VLA observation, nine NH_3 (9, 6) maser spots were resolved in this region; most of these spots are concentrated in the N1-K2-K3 region, while the brightest spot is located toward the N3 hot molecular core (Yan et al. 2022). In contrast, the maser emission of the organic molecular species presented in this work is found to be located close to the K4 centimeter-wave core and the K6 H II region, being spatially offset from the spots of the radiative pumping maser species OH and Class II CH_3OH. The 84 GHz CH_3OH maser displays a bright but extended distribution, centered around MS1 (near the K4 core), and subtending an angular size of $\sim 15''$. The emission tapers

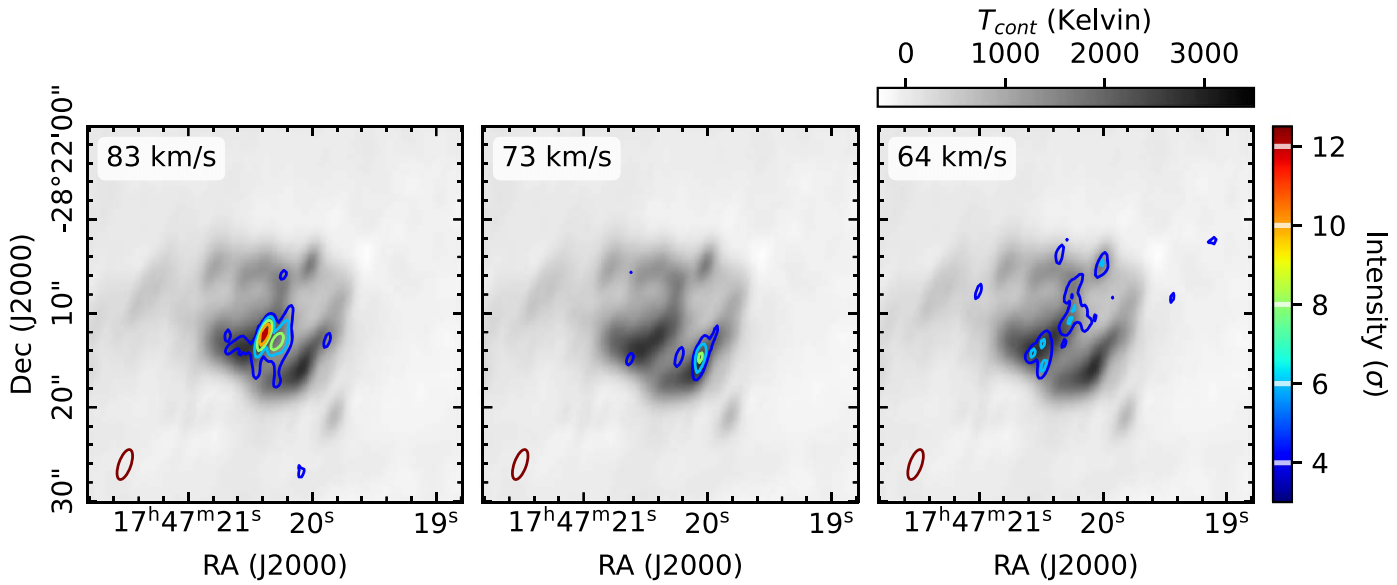

Figure 7. Peak intensity maps for each velocity component of the CH_2NH maser at 5.29 GHz superimposed on the continuum emission observed at 6.8 cm. The contour levels start at 4σ and continue up to the peak value with a step size of 2σ. The values of σ and peak values for the 83, 73, and 64 km s^{-1} components are 0.80, 0.93, and 0.85 mJy beam^{-1}, and 12.1, 8.86, and 6.60 mJy beam^{-1}, respectively.

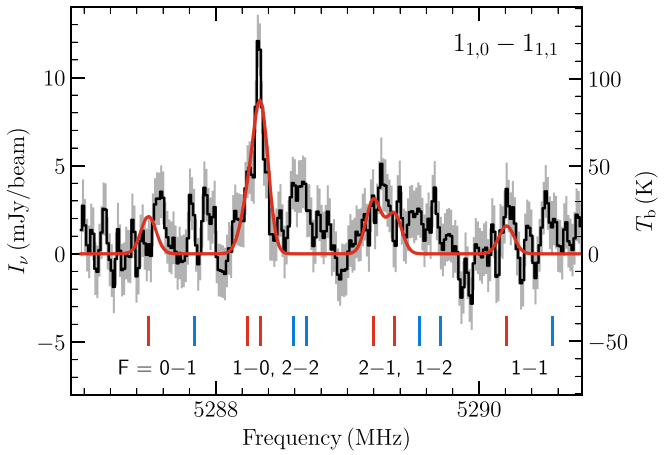

Figure 8. Observed spectrum of the CH_2NH $1_{1,0} - 1_{1,1}$ masing transition extracted toward MS2 is shown in black with noise levels shaded in gray. The synthetic spectrum with hyperfine splitting is overlaid in red for the 83 km s^{-1} components. The $F = 1 - 0$ and $2 - 2$ hyperfine components are blended. Each hyperfine component is denoted by a vertical bar, with the red bars corresponding to a V_{lsr} of 83 km s^{-1} and the blue bars corresponding to 64 km s^{-1} in blue.

off rapidly from the center with non-Gaussian profiles, a morphology possibly attributed to maser beaming effects.

We found that MS2, superimposed on the K6 H II region, harbors maser emission of both Class I CH_3OH at 84 GHz and CH_2NH at 5.29 GHz (Figure 11). The 83 km s^{-1} component of the CH_2NH maser at K6 remarkably resembles that of the Class I CH_3OH maser. Their consistent morphology serves as strong evidence to support a similar collisional pumping mechanism for the CH_2NH maser with the Class I CH_3OH maser as well as a common physical condition for triggering these masers. By understanding the conditions that are necessary for maser activities to occur, we can also better understand how they can be used to monitor astronomical objects. For example, since these masers are pumped by intense collisions, we can expect them to be good candidates for studying regions with time-dependent gas dynamics, such as episodic outflows from massive protostars. Future surveys of these new masers in addition to such objects are needed to determine how frequently they accompany Class I CH_3OH masers and how they might fit into proposed evolutionary time lines of masers in massive star formation (e.g., Ellingsen et al. 2012).

Alongside our observations of the Class I 84 GHz CH_3OH maser, we also examined the CH_3OH $8_0 - 7_1$ A-type transition at 95 GHz, which exhibits maser activity toward several famous star-forming regions, e.g., Orion-KL (Plambeck & Wright 1988), DR 21 (Plambeck & Menten 1990), and W51 (Pratap & Menten 1993). A recent single-dish survey of ATLASGAL clumps shows that the 84 GHz line is generally weaker than the 95 GHz line (Yang et al. 2023). In contrast, we found that the 95 GHz line exhibits weaker emission toward the identified maser spots in Sgr B2(N) compared to the 84 GHz line. The spatial distribution for the 95 GHz emission is similar to that for other thermal molecular lines, concentrating toward the N1 millimeter-wave source. This distribution may be attributed to either a weak maser or thermal radiation at different emission spots. It is noteworthy that Mehringer & Menten (1997) identified both maser and quasi-thermal emission components toward Sgr B2 in the 44 GHz line, a consecutive transition ($J = 6$) of the $(J + 1)_0 - J_1$ A series with the 95 GHz transition ($J = 7$). A more detailed analysis of other A-type CH_3OH transitions is needed to determine the nature of the 95 GHz emission.

5.3. Physical Conditions of Masing Clumps

The high spatial resolutions of interferometric observations enable us to resolve and segregate compact molecular emissions in diverse environments. In particular, the rich thermalized emission of CH_3OH and CH_2NH occurs in the hot core regions. In the N1 hot core, the ALMA observations reported an N_{col} of 2.0×10^{19} cm^{-2} for CH_3OH and 9.0×10^{17} cm^{-2} for CH_2NH at a T_{ex} of 230 K (Motiyenko et al. 2020; Margulès et al. 2022). In contrast, the bright

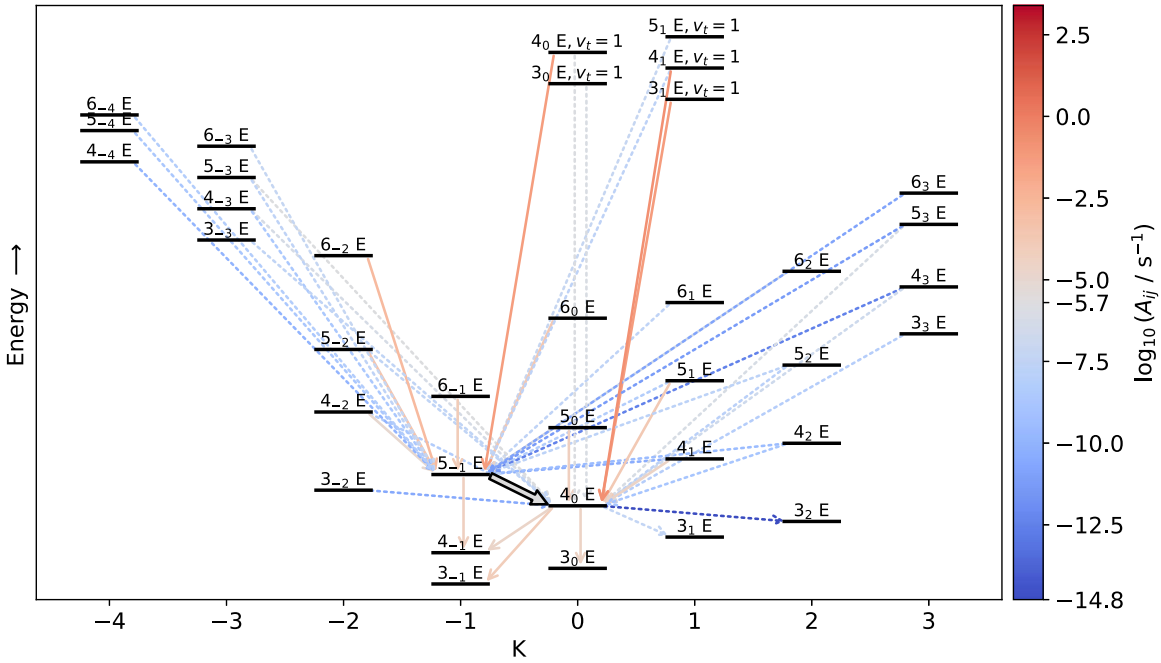

Figure 9. Energy level structure of the connected rotational transitions for the CH_3OH $5_{-1} - 4_0$ E transition. Energy levels are classified by the K quantum number and ordered by increasing energy but are not drawn to scale. The $\log_{10}\frac{A_{ij}}{s^{-1}}$ for each transition is shown with diverging color schemes, in which the critical middle value is set to be the $\log_{10}\frac{A_{ij}}{s^{-1}}$ of the $5_{-1} - 4_0$ E transition (−5.7). The targeted transitions are shown with gray arrows. Transitions with a smaller A_{ij} are shown as blue dotted lines, while transitions with a larger A_{ij} are shown as red solid lines.

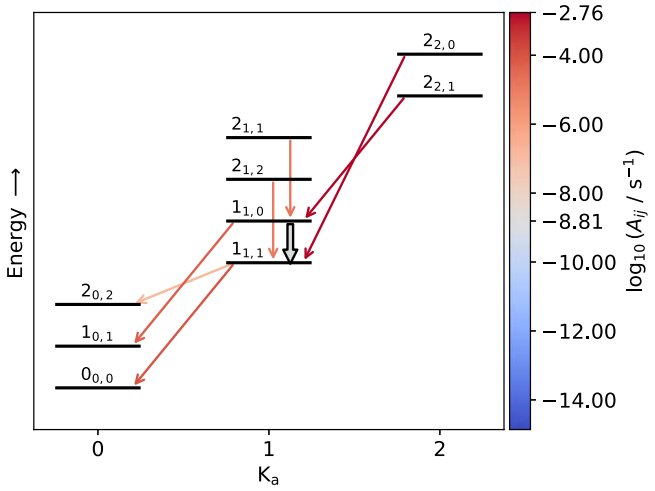

Figure 10. Energy level structure of the connected rotational transitions for CH_2NH $1_{1,0} - 1_{1,1}$ transition at 5288 MHz (thick gray arrow). Similar to Figure 9, but the critical middle value is set to be the $\log_{10}\frac{A_{ij}}{s^{-1}}$ of the $1_{1,0} - 1_{1,1}$ transition (−8.81).

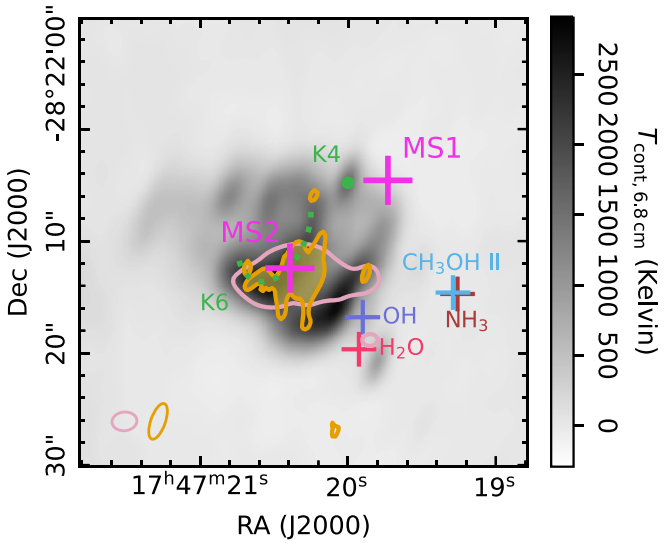

Figure 11. The 83 km s^{-1} components of the 84 GHz Class I CH_3OH maser and 5.29 GHz CH_2NH maser are shown with contours in pink and orange, respectively, and superimposed on the free–free continuum emission at 6.8 cm. Yellow shading indicates the overlap region where the CH_3OH emission exceeds 40σ and the CH_2NH emission exceeds 4σ. The 84 GHz Class I CH_3OH maser spots, MS1 and MS2, are marked with + symbols in magenta, while the brightest maser spots of OH, H_2O, NH_3, and Class II CH_3OH masers are marked in other colors (Argon et al. 2000; Caswell et al. 2010; Walsh et al. 2014; Yan et al. 2022). The K4 core and arc-like K6 H II region are marked with a green circle marker and dotted line, respectively.

stimulated maser emission of these two molecules concentrates in the less dense masing clumps. The N_{col} of these two molecules in the masing clumps (Tables 3 and 4) are 2–3 orders of magnitudes less abundant than those in the hot core.

From the MCMC analyses on the CH_3OH 84 GHz maser presented in Section 4.1, we found the T_k for the masing clumps to be ∼29–37 K. This range of T_k is consistent with the large-scale measurement of the Sgr B2 envelope from the OCS lines (30–37 K, Armijos-Abendaño et al. 2020) as well as the dust temperature of Sgr B2(N) obtained from Herschel observations (∼28 K, Etxaluze et al. 2013). It is also consistent with the value of T_k (30 K) derived from the non-LTE modeling of the weak masers of methyl formate detected in PRIMOS (Faure et al. 2014).

We also constrain the n_{H_2} of the masing clumps to be (5–8) × 10^4 cm^{-3}, a level significantly lower than that derived for

the hot core regions. The n_{H_2} of the Sgr B2(N) hot cores are $>10^7\,cm^{-3}$, with the N1 core reaching $\sim(1–2)\times10^9\,cm^{-3}$ (Sánchez-Monge et al. 2017). In contrast, the n_{H_2} of the masing clumps is comparable to the n_{H_2} of the colder envelope of Sgr B2, which is estimated to be 10^3–$10^4\,cm^{-3}$ based on the absorption molecular lines (Huettemeister et al. 1995; Schmiedeke et al. 2016). The slight enhancement in physical densities might be attributed to local energetic events occurring in the envelope necessary for a collisionally pumped maser.

This work presents a quantitative constraint on the physical conditions characterizing a masing clump of organic molecules. It serves as a reference for the physical conditions sufficient for exciting population inversion and collisionally pumped masers. These conditions include a T_k of ∼30, $n_{H_2} > 5\times10^4\,cm^{-3}$, and moderate molecular N_{col} ($>10^{16}\,cm^{-2}$ for CH_3OH and $>10^{14}\,cm^{-2}$ for CH_2NH). The relatively low values of temperatures and densities indicate that the masing clumps are situated in the colder and low-density external envelope. The distance from Sgr B2(N) to the edge of the external envelope is suggested to be approximately 19 pc (Schmiedeke et al. 2016). The continuum emission from Sgr B2(N) has an angular size of ∼10″, or 0.4 pc at a distance of 8.34 kpc (Reid et al. 2014), which subtends a solid angle of 3.5×10^{-4} sr to the envelope. This aligns with our assumption mentioned in Section 3.1, where background continuum emission sources are far from masing clumps, and therefore, do not significantly affect the local energy distribution of the molecules. Maser activities can manifest themselves in the presence of either a bright continuum background radiation or multiple chained masing clumps in the direction of a diffuse and weak background.

5.4. Caveat on Geometric Effects

Geometric effects related to the propagation of maser radiation become increasingly significant as the optical depth becomes lower than −1. Although `RADEX` and `molsim` support various geometries through escape probability approximation, other effects, such as maser beaming, are not treated. Such effects are particularly important in the case of unresolved clumps. The models also assume homogeneous physical conditions (i.e., one-zone models), which is inappropriate for very negative optical depths. For precisely modeling maser lines with strong amplification, a nonlocal treatment of radiation and level population is required.

Although our current treatment does not provide a precise solution, it is in principle appropriate for $|\tau|\ll1$ (the case of CH_2NH) and still offers a reasonable approximation to the first order as $|\tau|$ is of the order of unity (the case of CH_3OH). Incorporating corrections such as nonlocal treatments and other geometric effects would definitely improve the solution but it would also introduce significant computational costs. This becomes especially infeasible for MCMC calculations. The current solution represents the best that is achievable with our current resources, acknowledging that this approach is subject to future expansions and refinements.

6. Summary

We report interferometric observations of maser activity from organic molecules toward Sgr B2 using the ALMA and VLA. Enabled by the ALMA observations, we report the first detection of the Class I CH_3OH maser at 84 GHz toward Sgr B2. Multiple 84 GHz CH_3OH maser knots are discovered with the brightest spot MS1 located ∼3″ west of the K4 free–free continuum emission core. The peak brightness temperature of MS1 reaches 389.2 ± 0.2 K at a velocity of $58\,km\,s^{-1}$. In addition, another CH_3OH maser spot MS2 coexists with the K6 UC H II region at a velocity of $83\,km\,s^{-1}$. With the VLA observations, we resolve the 5.29 GHz CH_2NH maser emission into three velocity components. These three components display distinct fine-scale structures associated with the K5 and K6 bow-shaped H II regions. The $83\,km\,s^{-1}$ component is cospatial with MS2 and its peak brightness temperature has a lower limit of 121.8 ± 8.6 K.

We present a tool for modeling and fitting maser spectra with non-LTE calculations and a Bayesian approach. By leveraging the theoretical calculations on collisional rate coefficients and cross sections for both *E*-type CH_3OH and CH_2NH transitions, this fitting technique enables us to statistically constrain the physical conditions of the masing regions. In particular, our analysis suggests a two-chain-clump maser model for explaining the intense CH_3OH maser activity observed toward a region with weak and diffuse background radiation. This model can reproduce both the maser and the optically thick emission features of the CH_3OH spectra observed toward the brightest maser spot MS1.

Interferometric observations have not only enabled us to characterize the spatial origin and extent of maser emission but also helped to constrain the pumping mechanism through direct comparisons of their morphologies. We found a definite association between the maser emission from complex molecules and the K6 UC H II region. They are offset from the masing regions of the radiatively pumped maser species and the infrared sources. In contrast, the spatial correlation between the activities of the 84 GHz CH_3OH Class I maser and 5.29 GHz CH_2NH maser suggests that the CH_2NH maser is pumped by intense collisions, analogous to the Class I CH_3OH maser. By understanding the nature of the new maser species, which are pumped by intense collisions, we can better understand how they may serve as good candidates for studying and monitoring astronomical objects with time-dependent gas dynamics.

7. Data Access and Code

The code used to perform the analysis is part of the `molsim` open-source package; an archival version of the code can be accessed in Lee et al. (2023). The spectroscopic and collisional data for E-CH_3OH and CH_2NH can be found in the EMAA database (EMAA 2021).

Acknowledgments

B. A. M. and C. X. gratefully acknowledge the support of the National Science Foundation grant AST-2205126. This work was completed in part while C.X. was a Grote Reber Fellow. C.X. acknowledges support from the National Science Foundation through the Grote Reber Fellowship Program administered by Associated Universities, Inc./National Radio Astronomy Observatory and the Virginia Space Grant Consortium. The National Radio Astronomy Observatory is a facility of the National Science Foundation operated under cooperative agreement by Associated Universities, Inc. ALMA is a partnership of ESO (representing its member states), NSF (USA) and NINS (Japan), together with NRC (Canada), MOST

and ASIAA (Taiwan), and KASI (Republic of Korea), in cooperation with the Republic of Chile. The Joint ALMA Observatory is operated by ESO, AUI/NRAO and NAOJ. This paper makes use of the following ALMA data: ADS/JAO. ALMA#2011.0.00017.S. This research has made use of spectroscopic and collisional data from the EMAA database[12] (EMAA 2021). EMAA is supported by the Observatoire des Sciences de l'Univers de Grenoble (OSUG).

Facilities: ALMA, VLA, GBT

Software: `molsim` (Lee et al. 2023), `Emcee` (Foreman-Mackey et al. 2013), `Numba` (Lam et al. 2015), `CASA` (CASA Team et al. 2022),

Appendix A
Infrared Observations on Possible Associated Point Sources

We searched the point source catalog from both the 2MASS and the GLIMPSE program with the coordinate of MS1 ($\alpha_{J2000} = 17^h47^m19^s.73$, $\delta_{J2000} = -28°22'04''.58$). As shown in Figure A1, both 2MASS and GLIMPSE observations show that the nearest infrared source is located at $\alpha_{J2000} = 17^h47^m19^s.34$, $\delta_{J2000} = -28°22'05''.70$, $\sim 5''.2$ west of the maser spot. In addition, GLIMPSE detected another weak point source located toward $\alpha_{J2000} = 17^h47^m19^s.60$, $\delta_{J2000} = -28°22'06''.82$, $\sim 2''.8$ southwest of the maser spot.

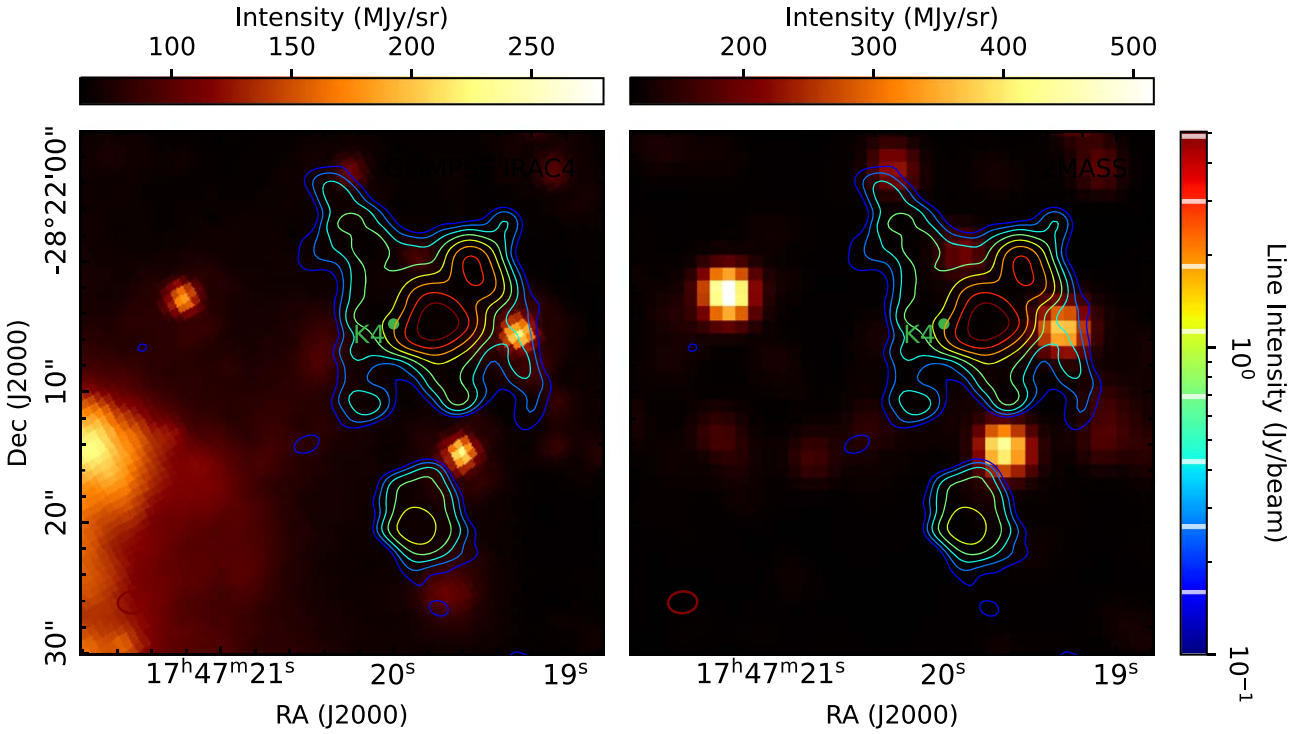

Figure A1. Infrared sources toward Sgr B2(N) reported by the GLIMPSE IRC 4 Band at 8.0 μm (Left) and the 2MASS K_s Band at 2.2 μm (right). The 84 GHz CH3OH maser emission at 58.5 km s^{-1} is shown with contours, as in Figure 2(r).

[12] https://emaa.osug.fr

Appendix B
MCMC Fitting Details

E-type CH_3OH. There are 11 free parameters in total to be adjusted in the MCMC analyses for *E*-type CH_3OH. For the spectra extracted toward MS1, the adopted prior and resultant posterior probability distributions for each parameter are depicted in Figure B1. The priors for V_{lsr} of both components are chosen to be a Gaussian distribution centered at $58.3\,km\,s^{-1}$ with a standard deviation of $2\,km\,s^{-1}$. Since the continuum is weak, as evidenced by the observations, we opted for a uniform prior distribution in the range of 2.725–15 K for T_{cont}. Meanwhile, all the remaining parameters have uninformative uniformly distributed priors. We found that the convergence rate of the RADEX algorithm slows down tremendously at high $N_{col} > 10^{17}\,cm^{-2}$. Therefore, we capped N_{col} at $10^{17.5}\,cm^{-2}$ and used 50,000 samples per walker (five times the value used for MS2). At high N_{col}, we observed deviations between the results obtained from our modified non-LTE algorithm and those from RADEX due to results not being converged in the latter.

A corner plot of the parameter covariances and their distribution for the MS1 MCMC fit is shown in Figure B2. As shown in Figure B1, we found that the optimal set of parameters converges to two peaks, each corresponding to one of the two scenarios (double maser and single maser). In particular, the peak at a lower velocity of the foreground component, corresponding to the higher velocity peak of the background component, corresponds to the double-maser scenario, while the other peak corresponds to the single-maser scenario. To better visualize the posteriors, we isolated the two peaks using $V_{lsr} = 58\,km\,s^{-1}$ as the criterion and plotted the posteriors separately in Figure B2. The corner plots with green and purple backgrounds correspond to the double-maser and single-maser scenarios, respectively.

In each corner, the first five parameters belong to the foreground component, while the last five are those of the background component. The 2D posterior distribution among parameters for the foreground component is shown in blue, while that for the background component is shown in red. The cross terms between the two components are shown in brown. The middle parameter is the background continuum temperature and the distribution between continuum temperature and other parameters is shown in yellow.

A similar MCMC analysis to that for the spectra extracted toward MS1 was carried out for the spectra extracted toward MS2. In contrast to Figure B1, the optimal set of parameters of MS2 converges to a single peak as shown in Figure 5. The corresponding corner plot of the parameter covariances and their distribution for the MS2 MCMC fit are shown in Figure B3. Similar to Figure B2, the parameters of the low-velocity component are shown in blue, while those of the high-velocity component are shown in red. We found that the MCMC analyses yield consistent results, regardless of whether the foreground or background velocity component is assigned as the high or low velocity along the LOS. Furthermore, the brown circular distribution, the cross terms between the two components, reveals that the two components are completely independent. This independence arises because the two components fit distinct portions of the spectrum because of their disparate central velocities compared with the line widths. In contrast, the strong degeneracy of the H_2 density and CH_3OH column density is revealed for each individual velocity component.

CH_2NH. An MCMC analysis with a one-clump model was carried out for the CH_2NH spectra. The prior and posterior distributions are shown in Figure B4, while a corner plot of the parameter covariances for the CH_2NH MCMC fit is shown in Figure B5.

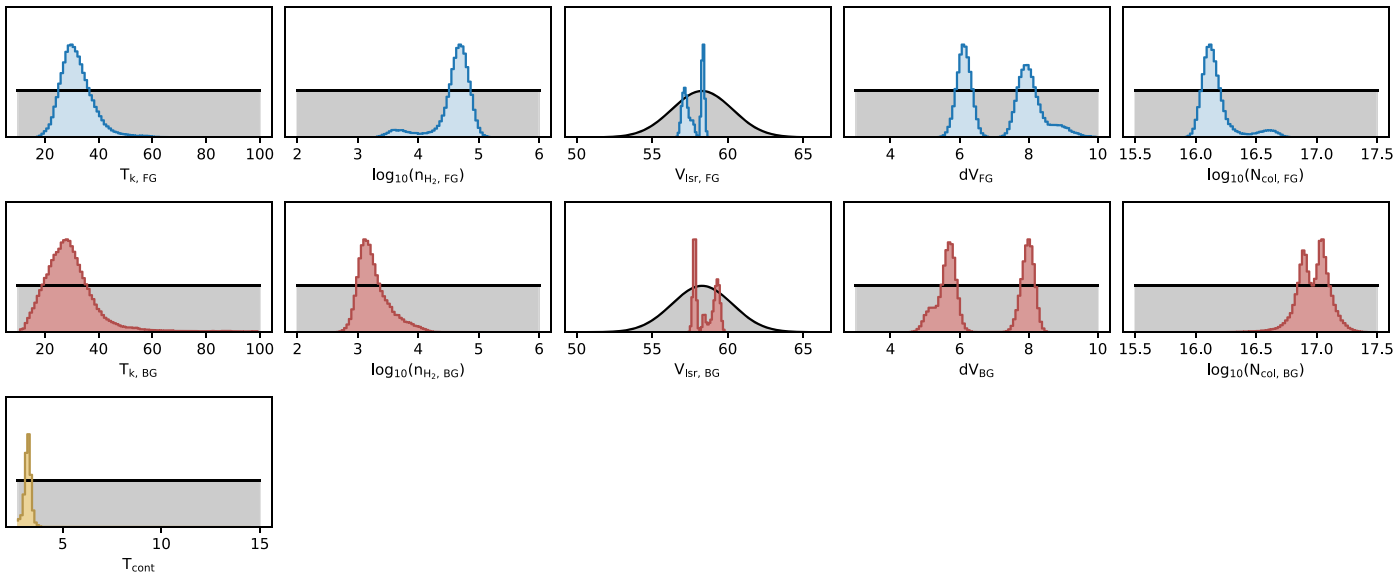

Figure B1. Prior and posterior distributions for the MCMC fit of CH_3OH *E*-type transitions toward MS1. The prior distribution of each parameter is shown in gray. The bimodal posterior distributions for the foreground component are shown in blue, whereas those for the background component are shown in red. The posterior of T_{cont} is shown in yellow.

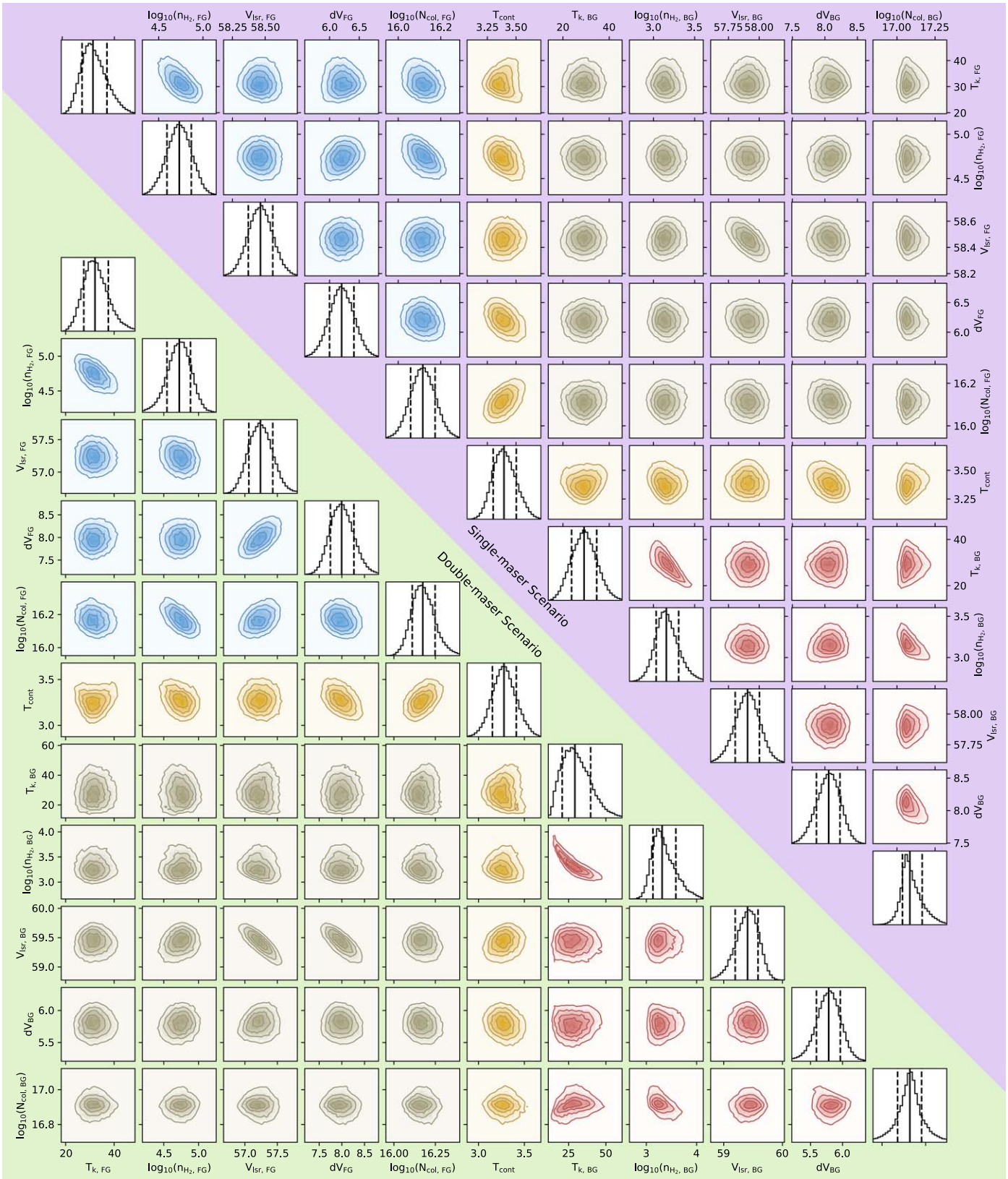

Figure B2. Parameter covariances and marginalized posterior distributions for the MCMC fit of CH_3OH *E*-type transitions toward MS1. The 16th, 50th, and 84th confidence intervals (corresponding to $\pm 1\sigma$ for a Gaussian posterior distribution) are shown as vertical lines. The distribution among the parameters for the foreground component is shown in blue and that for the background component is shown in red. The distribution among the parameters between the two components is shown in brown. The distribution between the background continuum temperature and other parameters is shown in yellow. To better visualize the bimodal posteriors, we isolated the two peaks and plotted separate posteriors for each, with the double-maser and single-maser scenarios highlighted by green and purple backgrounds respectively, as per the color scheme in Figure 4.

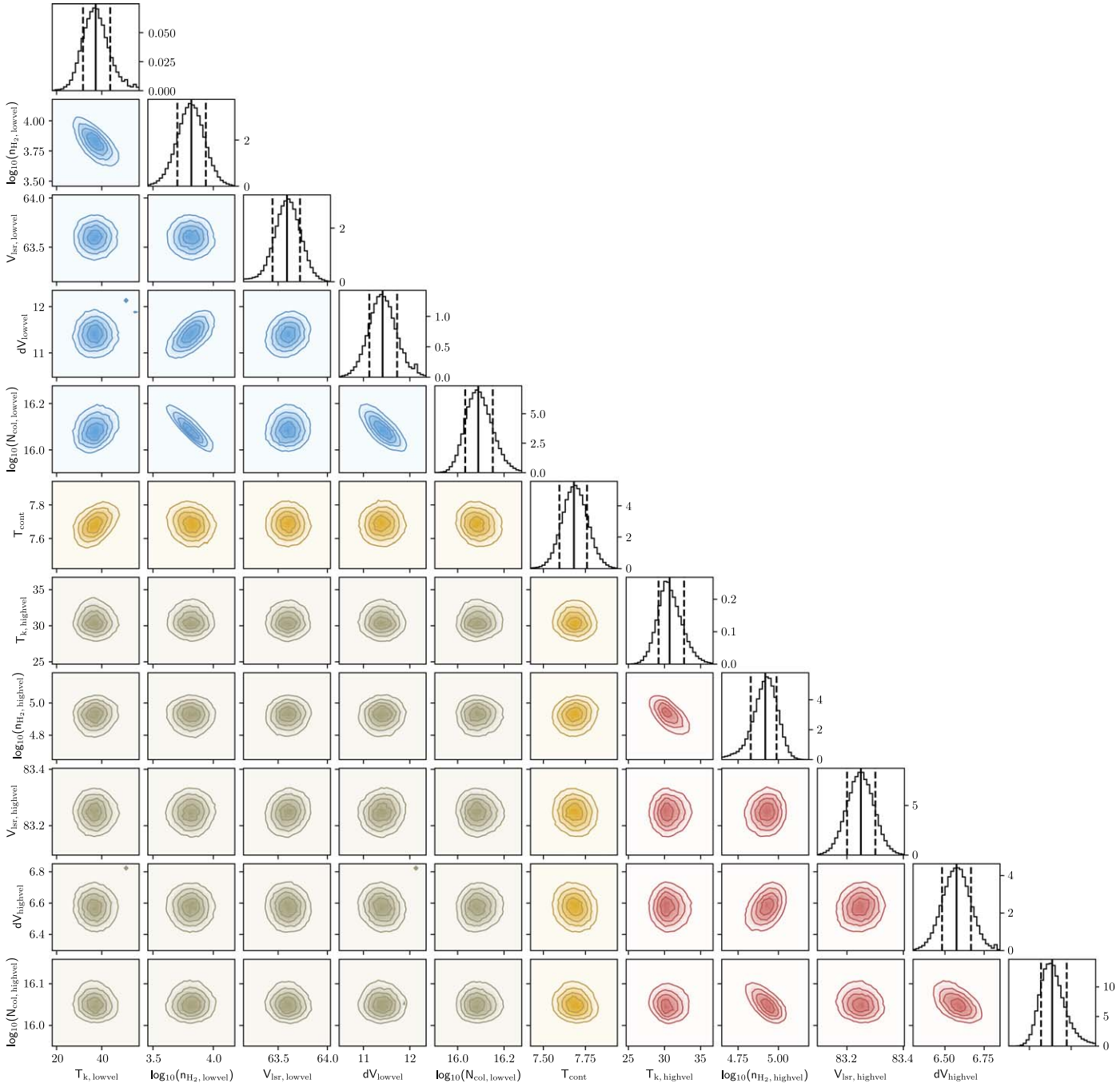

Figure B3. Similar to Figure B2, parameter covariances and marginalized posterior distributions for the MCMC fit of CH_3OH *E*-type transitions toward MS2. The distribution among the parameters for the low-velocity (64 km s^{-1}) component is shown in blue and that for the high-velocity (83 km s^{-1}) component is shown in red. The distribution among the parameters between the two components is shown in brown. The distribution between background continuum temperature and other parameters is shown in yellow.

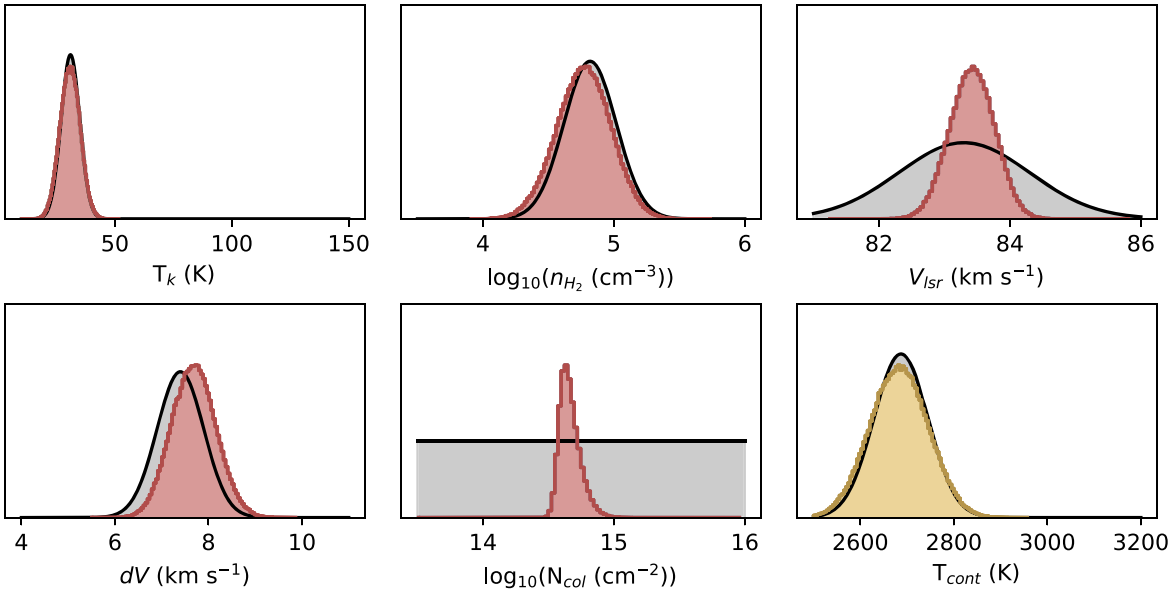

Figure B4. Prior and posterior distributions for the MCMC fit of the CH_2NH transitions toward MS2. The prior distribution for each parameter is shown in gray, while the priors on T_k and n_{H_2} are from the MCMC posteriors of CH_3OH in MS2 (Figure 5). The posterior distributions for the physical characteristics are shown in red, while the posterior for T_{cont} is shown in yellow.

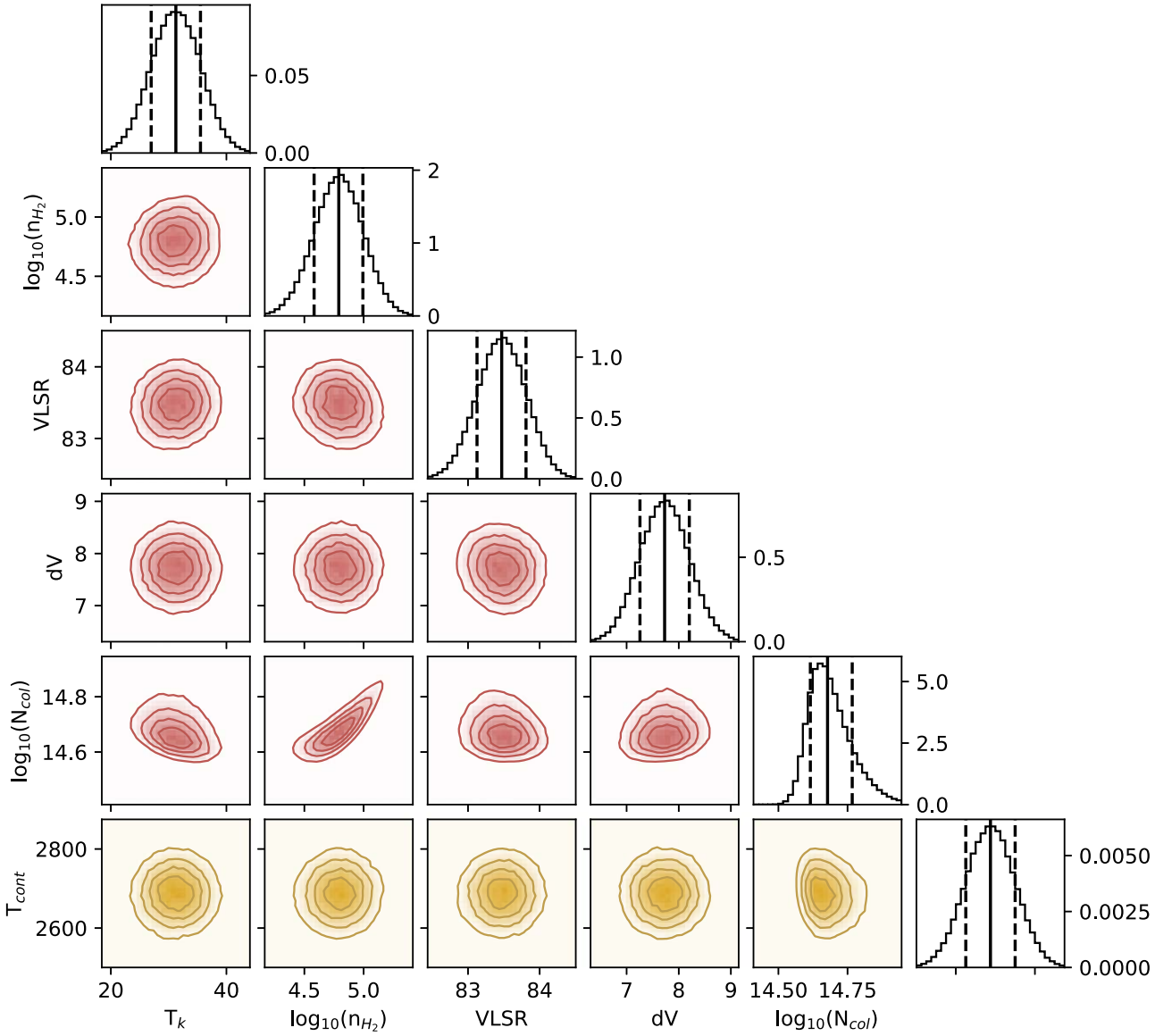

Figure B5. Parameter covariances and marginalized posterior distributions for the MCMC fit of the CH_2NH transitions. The 16th, 50th, and 84th confidence intervals (corresponding to $\pm 1\sigma$ for a Gaussian posterior distribution) are shown as vertical lines. The distribution among the parameters for the masing gas are shown in red and the distribution between background continuum temperature and other parameters is shown in yellow.

Appendix C
Collisional Rate Coefficient Calculations for CH_2NH

A first set of collisional data for CH_2NH + p-$H_2(j_2 = 0)$ was published by Faure et al. (2018) for applications to cold gas. The calculations of Faure et al. (2018) were performed for rotational transitions among the first 15 rotational levels of CH_2NH, i.e., up to the state $2_{2,0}$ ($j_1 = 2$, $K_a = 2$, $K_c = 0$) with an energy of 28.3 cm^{-1}. The full close-coupling method was used to generate rate coefficients at temperatures $5 \leqslant T_k \leqslant 30$ K and hyperfine-resolved rate coefficients were derived from the rotational rate coefficients using the statistical approximation; see Faure et al. (2018) for full details.

In this work, we have extended the calculations of Faure et al. (2018) to higher levels and temperatures and we have thus considered o-$H_2(j_2 = 1)$ as a second collider. Because close-coupling calculations are computationally very demanding when the temperature increases, we had recourse to the coupled-states approximation. As in Faure et al. (2018), all calculations were performed with the OpenMP extension[13] of version 14 of the `MOLSCAT` code (Hutson & Green 2012), using the same propagation parameters and rotational basis for CH_2NH ($j_1 \leqslant 12$) and p-H_2 ($j_2 = 0, 2$). The basis for o-H_2 was restricted to $j_2 = 1$ and the `MOLSCAT` parameter `EMAX` (used to limit basis functions to CH_2NH plus H_2 energies less than `EMAX`) was set to 1200 cm^{-1} for p-H_2 and 1318.64 cm^{-1} for o-H_2. The coupled-states calculations were performed for total energies between 2 and 800 cm^{-1} for p-H_2 and between 120 and 918 cm^{-1} for o-H_2. Rate coefficients were obtained for all rotational transitions among the first 49 levels, i.e., up to the state $8_{2,6}$ at 99.5 cm^{-1}, and for kinetic temperatures in the range of 10–150 K. Hyperfine-resolved rate coefficients were derived using the statistical approximation, as in Faure et al. (2018). Finally, the collisional data set was combined with the energy levels and radiative rates taken from the CDMS catalog (Müller et al. 2005) in order to provide an EMAA-formatted data file.

[13] http://ipag.osug.fr/~faurea/molscat/index.html

ORCID iDs

Ci Xue https://orcid.org/0000-0003-2760-2119
Anthony Remijan https://orcid.org/0000-0001-9479-9287
Alexandre Faure https://orcid.org/0000-0001-7199-2535
Emmanuel Momjian https://orcid.org/0000-0003-3168-5922
Todd R. Hunter https://orcid.org/0000-0001-6492-0090
Ryan A. Loomis https://orcid.org/0000-0002-8932-1219
Eric Herbst https://orcid.org/0000-0002-4649-2536
Brett McGuire https://orcid.org/0000-0003-1254-4817

References

Argon, A. L., Reid, M. J., & Menten, K. M. 2000, ApJS, 129, 159
Armijos-Abendaño, J., Banda-Barragán, W. E., Martín-Pintado, J., et al. 2020, MNRAS, 499, 4918
Batrla, W., Matthews, H. E., Menten, K. M., & Walmsley, C. M. 1987, Natur, 326, 49
Baudry, A., Forster, J. R., & Welch, W. J. 1974, A&A, 36, 217
Belloche, A., Müller, H. S. P., Garrod, R. T., & Menten, K. M. 2016, A&A, 587, A91
Bonfand, M., Belloche, A., Menten, K. M., Garrod, R. T., & Müller, H. S. P. 2017, A&A, 604, A60
Breen, S. L., Contreras, Y., Dawson, J. R., et al. 2019, MNRAS, 484, 5072
Breen, S. L., Ellingsen, S. P., Caswell, J. L., & Lewis, B. E. 2010, MNRAS, 401, 2219
Breen, S. L., Ellingsen, S. P., Contreras, Y., et al. 2013, MNRAS, 435, 524
CASA Team, Bean, B., Bhatnagar, S., et al. 2022, PASP, 134, 114501
Caswell, J. L. 1996, MNRAS, 283, 606
Caswell, J. L., Fuller, G. A., Green, J. A., et al. 2010, MNRAS, 404, 1029
Chen, X., Sobolev, A. M., Ren, Z.-Y., et al. 2020, NatAs, 4, 1170
Corby, J. F., Jones, P. A., Cunningham, M. R., et al. 2015, MNRAS, 452, 3969
Cragg, D. M., Sobolev, A. M., & Godfrey, P. D. 2002, MNRAS, 331, 521
Cragg, D. M., Sobolev, A. M., & Godfrey, P. D. 2005, MNRAS, 360, 533
Cyganowski, C. J., Brogan, C. L., Hunter, T. R., & Churchwell, E. 2009, ApJ, 702, 1615
Cyganowski, C. J., Brogan, C. L., Hunter, T. R., et al. 2012, ApJL, 760, L20
Elitzur, M., & Fuqua, J. B. 1989, ApJL, 347, L35
Ellingsen, S. P. 2006, ApJ, 638, 241
Ellingsen, S. P., Breen, S. L., Voronkov, M. A., et al. 2012, arXiv:1210.2139
EMAA 2021, Excitation of Molecules and Atoms for Astrophysics UGA, CNRS, CNRS-INSU, OSUG, doi:10.17178/EMAA
Etxaluze, M., Goicoechea, J. R., Cernicharo, J., et al. 2013, A&A, 556, A137
Faure, A., Lique, F., & Remijan, A. J. 2018, JPCL, 9, 3199
Faure, A., Remijan, A. J., Szalewicz, K., & Wiesenfeld, L. 2014, ApJ, 783, 72
Foreman-Mackey, D., Hogg, D. W., Lang, D., & Goodman, J. 2013, PASP, 125, 306
Forster, J. R., & Caswell, J. L. 1989, A&A, 213, 339
Fujisawa, K., Sugiyama, K., Motogi, K., et al. 2014, PASJ, 66, 31
Gargaud, M., Amils, R., Quintanilla, J. C., et al. 2011, Encyclopedia of Astrobiology (Berlin: Springer)
Gorski, M. D., Aalto, S., Mangum, J., et al. 2021, A&A, 654, A110
Hoffman, I. M., Goss, W. M., & Palmer, P. 2007, ApJ, 654, 971
Huettemeister, S., Wilson, T. L., Mauersberger, R., et al. 1995, A&A, 294, 667
Humire, P. K., Henkel, C., Hernández-Gómez, A., et al. 2022, A&A, 663, A33
Hunter, T. R., Brogan, C. L., Bartkiewicz, A., et al. 2018, in ASP Conf. Ser. 517, Science with a Next Generation Very Large Array, ed. E. Murphy (San Francisco, CA: ASP), 321
Hutson, J. M., & Green, S. 2012, MOLSCAT: MOLecular SCATtering, Astrophysics Source Code Library, ascl:1206.004
Kartje, J. F., Königl, A., & Elitzur, M. 1999, ApJ, 513, 180
Lam, S. K., Pitrou, A., & Seibert, S. 2015, in Proc. Second Workshop on the LLVM Compiler Infrastructure in HPC (New York: ACM), 1
Lee, K. L. K., Loomis, R. A., Xue, C., El-Abd, S., & McGuire, B. A. 2023, molsim, v0.4.0, Zenodo, doi:10.5281/zenodo.8118192
Lees, R. M. 1973, ApJ, 184, 763
Leurini, S., Menten, K. M., & Walmsley, C. M. 2016, A&A, 592, A31
Margulès, L., Remijan, A., Belloche, A., et al. 2022, A&A, 663, A132
Mather, J. C., Fixsen, D. J., Shafer, R. A., Mosier, C., & Wilkinson, D. T. 1999, ApJ, 512, 511
McCarthy, T. P., Ellingsen, S. P., Breen, S. L., Voronkov, M. A., & Chen, X. 2018, ApJL, 867, L4
McGrath, E. J., Goss, W. M., & De Pree, C. G. 2004, ApJS, 155, 577
McGuire, B. A., Loomis, R. A., Charness, C. M., et al. 2012, ApJL, 758, L33
Mehringer, D. M., & Menten, K. M. 1997, ApJ, 474, 346
Menten, K. M. 1991, in ASP Conf. Ser. 16, Atoms, ions and molecules: New results in spectral line astrophysics, ed. A. D. Haschick & P. T. P. Ho (San Francisco, CA: ASP), 119
Morita, K.-I., Hasegawa, T., Ukita, N., Okumura, S. K., & Ishiguro, M. 1992, PASJ, 44, 373
Moscadelli, L., Sánchez-Monge, Á., Goddi, C., et al. 2016, A&A, 585, A71
Motiyenko, R. A., Belloche, A., Garrod, R. T., et al. 2020, A&A, 642, A29
Müller, H. S. P., Schlöder, F., Stutzki, J., & Winnewisser, G. 2005, JMoSt, 742, 215
Plambeck, R. L., & Menten, K. M. 1990, ApJ, 364, 555
Plambeck, R. L., & Wright, M. C. H. 1988, ApJL, 330, L61
Pratap, P., & Menten, K. 1993, Interferometric observations of 95 GHz methanol masers, Vol. 412 (Berlin: Springer), 211
Qiao, H., Li, J., Shen, Z., Chen, X., & Zheng, X. 2014, MNRAS, 441, 3137
Qiao, H.-H., Walsh, A. J., Breen, S. L., et al. 2018, ApJS, 239, 15
Rabli, D., & Flower, D. R. 2010, MNRAS, 406, 95
Reid, M. J., Menten, K. M., Brunthaler, A., et al. 2014, ApJ, 783, 130
Reid, M. J., Menten, K. M., Brunthaler, A., et al. 2019, ApJ, 885, 131
Remijan, A., Xue, C., Margulès, L., et al. 2022, A&A, 658, A85
Sanna, A., Moscadelli, L., Cesaroni, R., et al. 2016, A&A, 596, L2
Sánchez-Monge, Á., Schilke, P., Schmiedeke, A., et al. 2017, A&A, 604, A6
Schmiedeke, A., Schilke, P., Möller, T., et al. 2016, A&A, 588, A143
Sobolev, A. M., Cragg, D. M., & Godfrey, P. D. 1997, A&A, 324, 211
Sobolev, A. M., & Deguchi, S. 1994, A&A, 291, 569
Song, S.-M., Chen, X., Shen, Z.-Q., et al. 2022, ApJS, 258, 19
Szymczak, M., Pillai, T., & Menten, K. M. 2005, A&A, 434, 613
Towner, A. P. M., Brogan, C. L., Hunter, T. R., et al. 2017, ApJS, 230, 22
van der Tak, F. F. S., Black, J. H., Schöier, F. L., Jansen, D. J., & van Dishoeck, E. F. 2007, A&A, 468, 627
Voronkov, M. A., Brooks, K. J., Sobolev, A. M., et al. 2006, MNRAS, 373, 411
Voronkov, M. A., Caswell, J. L., Ellingsen, S. P., Green, J. A., & Breen, S. L. 2014, MNRAS, 439, 2584
Walsh, A. J., Macdonald, G. H., Alvey, N. D. S., Burton, M. G., & Lee, J. K. 2003, A&A, 410, 597
Walsh, A. J., Purcell, C. R., Longmore, S. N., et al. 2014, MNRAS, 442, 2240
Xu, Y., Li, J. J., Hachisuka, K., et al. 2008, A&A, 485, 729
Xue, C., Remijan, A. J., Burkhardt, A. M., & Herbst, E. 2019, ApJ, 871, 112
Yan, Y. T., Henkel, C., Menten, K. M., et al. 2022, A&A, 666, L15
Yang, W., Gong, Y., Menten, K. M., et al. 2023, A&A, 675, A112